

Numerical investigation of the hydrodynamics of anguilliform swimming in the transitional and inertial flow regimes

Iman Borazjani and Fotis Sotiropoulos*

St Anthony Falls Laboratory, Department of Civil Engineering, University of Minnesota, Minneapolis, MN 55402, USA

*Author for correspondence (e-mail: fotis@umn.edu)

Accepted 15 November 2008

SUMMARY

We employ numerical simulation to investigate the hydrodynamic performance of anguilliform locomotion and compare it with that of carangiform swimming as the Reynolds number (Re) and the tail-beat frequency (Strouhal number, St) are systematically varied. The virtual swimmer is a 3-D lamprey-like flexible body undulating with prescribed experimental kinematics of anguilliform type. Simulations are carried out for three Reynolds numbers spanning the transitional and inertial flow regimes, $Re=300$, 4000 (viscous flow), and ∞ (inviscid flow). The net mean force is found to be mainly dependent on the tail-beat frequency rather than the tail-beat amplitude. The critical Strouhal number, St^* , at which the net mean force becomes zero (constant-speed self-propulsion) is, similar to carangiform swimming, a decreasing function of Re and approaches the range of St numbers at which most anguilliform swimmers swim in nature ($St \sim 0.45$) only as Re increases. The anguilliform swimmer's force time series is characterized by significantly smaller fluctuations above the mean than that for carangiform swimmers. In stark contrast with carangiform swimmers, the propulsive efficiency of anguilliform swimmers at St^* is not an increasing function of Re but instead is maximized in the transitional regime. Furthermore, the power required for anguilliform swimming is less than that for the carangiform swimmer at the same Re . We also show that the form drag decreases while viscous drag increases as St increases. Finally, our simulations reinforce our previous finding for carangiform swimmers that the 3-D wake structure depends primarily on the Strouhal number.

Key words: fish swimming, numerical simulations, anguilliform, carangiform, lamprey, energetics, wake structure.

INTRODUCTION

More than 88% of fishes use body/caudal fin (BCF) undulations for propulsion (Videler, 1993; Borazjani and Sotiropoulos, 2008). The BCF propulsion has been categorized into four different types, or modes, of swimming (Lindsey, 1978; Sfakiotakis et al., 1999): anguilliform, sub-carangiform, carangiform and thunniform. In this paper we focus on the anguilliform mode of swimming and compare its hydrodynamic performance with that of the carangiform mode we studied in our previous work (Borazjani and Sotiropoulos, 2008).

Anguilliform swimmers differ from carangiform swimmers in body morphology and body undulations. They typically have long narrow bodies, and the width of the body remains almost constant from head to tail. By contrast, carangiform swimmers have thicker bodies, with their body width decreasing at the peduncle where the body attaches to the caudal fin. Anguilliform swimmers undulate most of their body *via* a backward travelling wave whose amplitude is large over the entire body length. For carangiform swimmers, the large-amplitude body undulations are restricted to one-half or even one-third of the posterior part of the body, and the undulation amplitude increases sharply in the caudal area. The wavelength of the traveling wave is usually lower for anguilliform swimmers (about 70% of body length) than for carangiform swimmers (about one body length) (Videler and Wardle, 1991). The two non-dimensional parameters that characterize steady inline undulatory swimming, regardless of its specific mode, are the flow Reynolds number (Re) and the Strouhal number (St) of the undulatory body motion, which can

be defined as follows (Triantafyllou et al., 2000; Lauder and Tytell, 2006):

$$Re = UL/\nu, \quad (1)$$

$$St = fA/U. \quad (2)$$

In the above equations, L is the fish length, U is the steady inline swimming speed, ν is the kinematic viscosity of the water, A is the width of the wake, which is approximated by the maximum lateral excursion of the tail over a cycle, and f is the tail-beat frequency.

Early work on anguilliform swimming dates back to Gray (Gray, 1933a; Gray, 1933b), who was the first to study the body movement of eels and their propulsive mechanism. He was the first to show that the body undulations have the form of a backward traveling wave. More recent studies employ the state-of-the-art particle image velocimetry (PIV) technique and digital cameras to study swimming. Muller et al. reported that anguilliform swimmers shed two vortices per half tail-beat cycle, which organize themselves into two distinct rows of vortices (the so-called double-row wake) (Muller et al., 2001). Tytell and Lauder report a similar wake (Tytell and Lauder, 2004) and calculate the swimming performance using Lighthill's elongated body theory (Lighthill, 1960). Carling and Williams have carried out 2-D self-propelled simulations of eel swimming, but the wake structure did not match the experimental results (Carling and Williams, 1998). However, this discrepancy has been resolved by performing 3-D simulations and pointing out that the 2-D simulations are not able to capture the actual 3-D flow

field (Kern and Koumoutsakos, 2006). Fish larvae have also been studied experimentally since their wakes resemble that of an eel but tend to die off very rapidly due to the low Re and high viscous effects (Muller et al., 2008). For a review of carangiform swimming, the reader is referred to our previous work (Borazjani and Sotiropoulos, 2008).

The differences in body morphology and kinematics of anguilliform and carangiform swimmers should be expected to lead to differences in hydrodynamic performance. In fact, according to Lighthill's elongated body theory (EBT) (Lighthill, 1970), carangiform swimmers should have higher efficiency. This is because, according to the EBT, thrust is only produced at the tail, and consequently the large undulation amplitudes along the entire body of anguilliform swimmers produce power that is wasted. As a result of this theoretical argument, the prevailing wisdom is that carangiform swimmers are more efficient than anguilliform swimmers. However, it is important to keep in mind that the EBT is inviscid and thus inherently incapable of accounting for the effect of Reynolds number on swimming efficiency. Nevertheless, this notion regarding the superior efficiency of carangiform swimmers has not been proven or disproven experimentally, presumably due to inherent methodological difficulties encountered when attempting to estimate efficiency and power output of self-propelled bodies, and specifically fishes, through experiments – see Tytell's thorough review for the challenges confronting experimental studies with live fish (Tytell, 2007). Perhaps the most important such difficulty stems from the lack of control over live fish, which precludes the systematic variation of governing parameters. Even if similar conditions and total control over live fish could be achieved in experiments, it would still be challenging to estimate swimming performance, since obtaining 3-D flow measurements around a swimming fish is far from straightforward. As pointed out by Tytell, the state-of-the-art PIV technique for measuring velocities can only provide measurements on 2-D planes while accurate estimation of swimming performance requires the full 3-D velocity field (Tytell, 2007). Furthermore, the pressure field, which is also needed to determine the hydrodynamic forces (Dabiri, 2005), is not easy to measure.

As we showed in our previous paper (Borazjani and Sotiropoulos, 2008), numerical simulations can be used to circumvent many of the aforementioned difficulties. Carefully designed numerical experiments with fully controllable virtual swimmers can be used to systematically vary governing parameters and elucidate many important issues pertaining to the hydrodynamics of swimming over a wide range of flow regimes and body kinematics. In a previous paper (Borazjani and Sotiropoulos, 2008), we focused on the hydrodynamics of carangiform locomotion using a virtual swimmer closely modeled after the body of a mackerel. In the current paper, we adopt our previous approach (Borazjani and Sotiropoulos, 2008) to carry out a systematic investigation of the hydrodynamics of anguilliform swimming over a range of Reynolds numbers and Strouhal numbers. Our findings are juxtaposed with those of our previous study (Borazjani and Sotiropoulos, 2008) to highlight the similarities and differences between the anguilliform and carangiform modes of swimming and are also compared with previous experimental findings available in the literature. We employ an anatomically realistic model of a lamprey body reconstructed from a detailed computed tomography (CT) scan of an actual lamprey. Even though our method can easily handle an anatomically realistic lamprey, in this work all fins are neglected due to lack of detailed kinematic data, and only the main body is retained in the model. Such geometric simplification will of course affect the small-scale vortices shed by the various fins but the

resulting simplified model is comparable in complexity to that of the carangiform swimmer we studied in our previous work. The anguilliform kinematics are prescribed using available experimental data (Hultmark et al., 2007), and the virtual swimmer is assumed to be swimming along a straight line at constant speed in a uniform ambient flow. The flow induced by the body undulations is calculated by solving the unsteady 3-D Navier–Stokes equations using the hybrid Cartesian/immersed-boundary (HCIB) method developed by our group (Gilmanov and Sotiropoulos, 2005; Ge and Sotiropoulos, 2007; Borazjani et al., 2008). Calculations are carried out on fine computational meshes to ensure sufficient numerical resolution of the viscous region near the fish body. Similar to our previous work for carangiform swimmers (Borazjani and Sotiropoulos, 2008), viscous flow simulations are carried out at two Reynolds numbers, $Re=300$ and 4000 . Inviscid calculations are also carried out, representing the flow in the limit of infinite Reynolds number ($Re=\infty$). For all three cases, the Strouhal number is varied systematically, starting from zero (rigid body case), while the swimming speed, U (i.e. the Reynolds number), is held constant. Note that, as in our previous work (Borazjani and Sotiropoulos, 2008), in order to be able to vary the Strouhal number while maintaining U constant we simulate the flow induced by an undulating fish that is attached to and towed by a rigid tether that translates the fish in a stagnant fluid at constant velocity U . By fixing the speed of the tether, U , we can obtain the desired value of Re . The Strouhal number is adjusted by changing the fish tail-beat frequency f – i.e. by assuming that our virtual swimmer is trained to always undulate its tail at the desired constant frequency. For any given combination of the so-obtained Re and St , the simulated flow field is used to calculate the force F exerted on the fish body by the flow. If $F \neq 0$, the excess force is absorbed by the hypothetical tether so that the net force acting on the fish is always zero and the constant swimming velocity assumption is satisfied. In such cases, if the hypothetical tether is instantaneously severed, the fish will either accelerate forward or decelerate backward under the action of the excess force F . For a given Reynolds number, we vary the Strouhal number until the net mean force acting on the fish is zero, $F=0$. For such a case, the numerical tether has obviously no effect on the fish since if it is severed the fish will continue swimming at constant speed U . Via this procedure we are able to find, for a given Reynolds number, the Strouhal number for which steady, inline swimming is possible. The computed results are analyzed to elucidate several important aspects of anguilliform swimming and are compared with those for carangiform swimming under similar conditions. These include, among others, the ability of anguilliform kinematics vs carangiform kinematics to produce thrust as a function of Reynolds number, the swimming efficiency and propulsive power requirements in the transitional and inertial regimes, and the 3-D structure of the wake as a function of Re and St .

The paper is organized as follows. First, we briefly describe the numerical method and present the details of the fish model and prescribed kinematics. Second, we discuss the numerical experiments of the anguilliform swimmer and compare it with the carangiform swimmer in terms of hydrodynamic forces, drag increase/reduction, swimming efficiency and the 3-D vortical structures in the wake. Finally, we summarize our findings, present the conclusions of this work and outline the areas for future research.

MATERIALS AND METHODS

The numerical method

The numerical method is identical to that used in our previous work on carangiform swimming (Borazjani and Sotiropoulos, 2008), and

the readers are referred to that paper and other papers from our group for more details (Gilmanov and Sotiropoulos, 2005; Ge and Sotiropoulos, 2007; Borazjani et al., 2008). In summary, we solve the unsteady 3-D incompressible Navier–Stokes equations in a Cartesian domain that contains the flexible fish body using the HCIB method (Gilmanov and Sotiropoulos, 2005). The method employs an unstructured, triangular mesh to discretize and track the position of the fish body. Boundary conditions for the velocity field at the Cartesian grid nodes that are exterior to but in the immediate vicinity of the immersed boundary [immersed boundary (IB) nodes] are reconstructed by linear or quadratic interpolating along the local normal to the boundary. No explicit boundary conditions are required for the pressure field at the IB nodes due to the hybrid staggered/non-staggered mesh formulation of Gilmanov and Sotiropoulos (Gilmanov and Sotiropoulos, 2005). The HCIB reconstruction method has been shown to be second-order accurate on Cartesian grids with moving immersed boundaries (Gilmanov and Sotiropoulos, 2005). The IB nodes at each time step are identified using an efficient ray-tracing algorithm (Borazjani et al., 2008). The governing equations are solved using the efficient fractional step method of Ge and Sotiropoulos (Ge and Sotiropoulos, 2007). The Poisson equation for the pressure is solved with the FGMRES method (Saad, 2003), enhanced with multigrid as preconditioner using the parallel libraries of PETSc (Satish Balay et al., 2001). For more details, the reader is referred to our previous papers (Ge and Sotiropoulos, 2007; Borazjani et al., 2008).

The numerical method has been validated extensively (Gilmanov and Sotiropoulos, 2005; Borazjani and Sotiropoulos, 2008) for flows with moving boundaries and has also been applied successfully to simulate fish-like swimming (Gilmanov and Sotiropoulos, 2005; Borazjani and Sotiropoulos, 2008).

Fish body kinematics and non-dimensional parameters

The virtual anguilliform swimmer was created from a lamprey CT scan by Professor Frank Fish, provided to us by Professor Lex Smits from Princeton University. The experimental data were only available for the main body of the lamprey and, as such, all the fins were neglected. The model is meshed with triangular elements as required for implementing the HCIB method (Fig. 1).

The kinematics for anguilliform swimmers is generally in the form of a backward traveling wave, with the wave amplitude increasing almost linearly from the head to the tail of the fish (Gray, 1933b). The equation describing the lateral undulations of the fish body is given as follows (all lengths are non-dimensionalized with the fish length, L):

$$h(z,t) = a(z) \sin(kz - \omega t), \quad (3)$$

where z is the axial (flow) direction measured along the fish axis from the tip of the fish's snout; $h(z,t)$ is the lateral excursion of the body at time t ; $a(z)$ is the amplitude envelope of lateral motion as a function of z ; k is the wave number of the body undulations that corresponds to a wavelength λ ; and ω is the angular frequency.

The four important non-dimensional similarity parameters in fishlike swimming are: (1) the Reynolds number based on L , the swimming speed U , and the fluid kinematic viscosity ν ($Re=LU/\nu$); (2) the Strouhal number based on the maximum lateral excursion of the tail, $A=2h_{max}$, and the tail-beat frequency f ($St=2fh_{max}/U$); (3) the non-dimensional wavelength λ/L ; and (4) the non-dimensional amplitude envelope $a(z)/L$. Sometimes, the so-called slip velocity or slip ratio, defined as $\beta=U/V=U/(\omega/k)$, is used instead of non-dimensional wavelength. Using either parameter is correct.

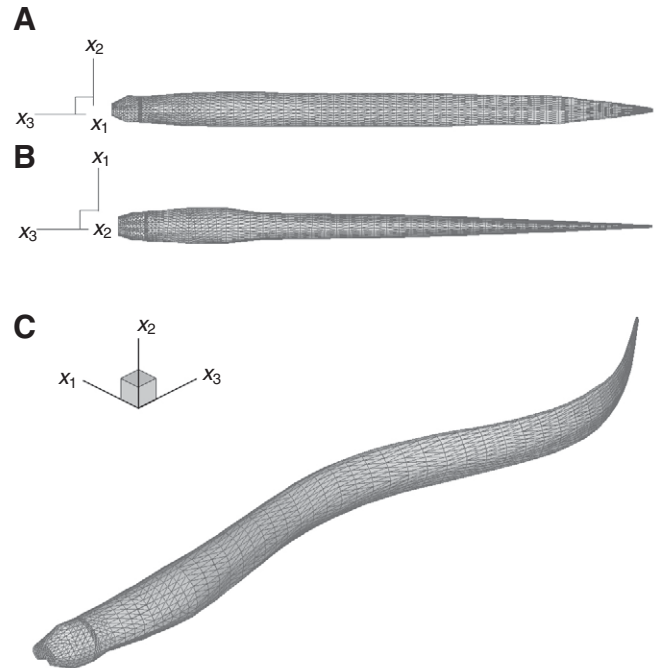


Fig. 1. The anguilliform virtual swimmer, created from a CT scan of a lamprey and meshed with triangular elements as needed by the sharp-interface immersed boundary method, from (A) side view, (B) top view and (C) perspective.

However, the slip velocity varies with the tail-beat frequency while the wavelength and the tail-beat frequency are independent.

In all our simulations, the λ/L and the $a(z)$ parameters, hereafter referred to as shape parameters, are specified such that the fish body motion is similar to the typical anguilliform swimmers' body motion. The amplitude envelope $a(z)$ can be approximated by an exponential function (Tytell and Lauder, 2004):

$$a(z) = a_{max} e^{z-1}, \quad (4)$$

where the coefficient a_{max} gives the maximum amplitude at the tail ($z=1$). For a typical lamprey, a_{max} is set equal to 0.089 (Hultmark et al., 2007). The wave number k in all the simulations is based on the non-dimensional wavelength $\lambda/L=0.642$, as in Hultmark et al. (Hultmark et al., 2007). The non-dimensional angular frequency used in Eqn3 is calculated based on the Strouhal number as follows:

$$\omega = 2\pi f L / U = 2\pi St / 2a_{max}. \quad (5)$$

The above non-dimensional angular frequency ω is used along with the non-dimensional time tU/L in Eqn3. Fig. 2 shows the midlines of the fish calculated at several time instants during one tail-beat cycle using Eqn3, with the amplitude envelope calculated by Eqn4, and the coefficients and shape parameters obtained from anguilliform swimming experiments (Hultmark et al., 2007). Fig. 1C shows one instant of such undulations imposed on the lamprey body.

Computational grid and other details

As we already explained in the introduction and in accordance with our previous work (Borazjani and Sotiropoulos, 2008), in all our simulations the anguilliform virtual swimmer is attached to a rigid tether and is being towed at constant velocity U . Therefore, all the equations are solved in the inertial frame moving with constant velocity U attached to the fish. The computational domain is a

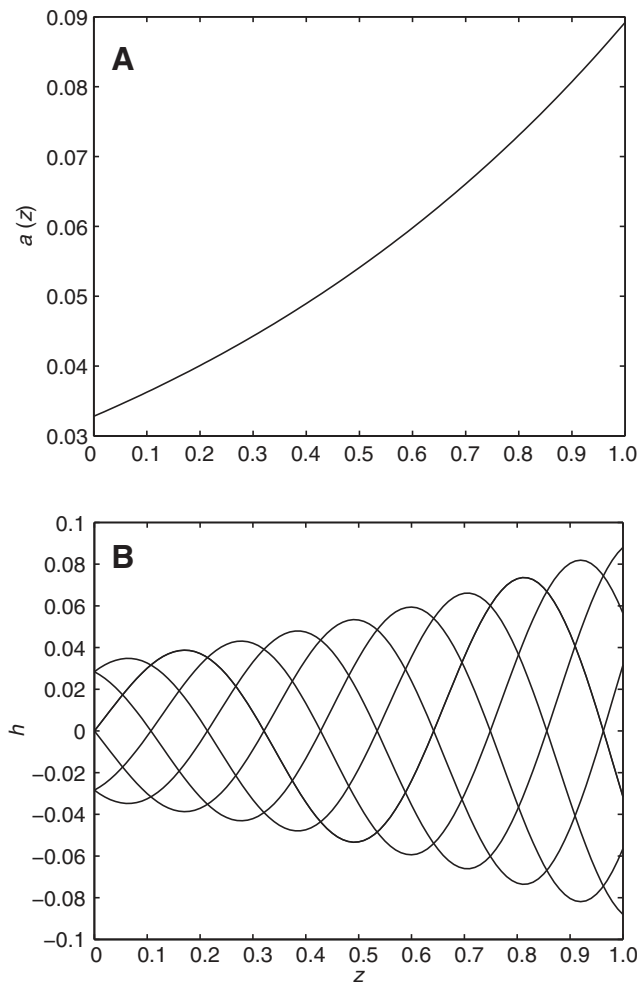


Fig. 2. (A) The amplitude envelope for the virtual anguilliform swimmer and (B) midlines of the virtual anguilliform swimmer according to Eqn3 for several time instants during one tail-beat cycle.

$2L \times L \times 7L$ cuboid, which is discretized with 5.5 million grid nodes, as in Borazjani and Sotiropoulos (Borazjani and Sotiropoulos, 2008). The domain width $2L$ and height L are more than 15 times the fish width ($0.067L$) and fish height ($0.066L$), respectively. A uniform mesh with constant spacing $\Delta x_3 = 0.008L$ in length, $\Delta x_2 = 0.002L$ in height, and $\Delta x_1 = 0.004L$ in width is used to discretize an inner cuboid with dimensions $0.2L \times 0.08L \times L$ enclosing the fish at all times. The mesh is stretched from the faces of this smaller inner cuboid to the boundaries of the computational domain using a hyperbolic tangent stretching function. Note that since the anguilliform swimmer's body is thinner relative to that of the carangiform swimmer, the inner cuboid is smaller for the anguilliform swimmer, and smaller spacing has been used in order to ensure a similar number of grid nodes along the width and height of the anguilliform swimmer relative to the carangiform one. The tail-beat period, τ , is divided in 180 time steps, i.e. $\Delta t = \tau/180$, which is slightly smaller than that we used for the carangiform simulations (Borazjani and Sotiropoulos, 2008) due to finer mesh size in the x_1 and x_2 directions. The fish is placed $1.5L$ from the inlet plane in the axial direction and centered in the transverse and vertical directions. At the outer boundaries of the computational domain, the following boundary conditions are used: uniform flow at the

inlet plane, slip wall condition at the lateral boundaries, and Neumann boundary condition at the outlet.

The grid sensitivity of our numerical simulations has already been addressed in detail (Borazjani and Sotiropoulos, 2008) and, as such, it will not be further discussed herein. Here it suffices to state that, based on the extensive numerical sensitivity studies we carried out in our previous work for carangiform swimming, the size of the computational mesh and time increment employed in the present simulations are adequate for obtaining results that are insensitive to further refinement of numerical parameters.

Calculation of hydrodynamic forces and swimming efficiency

The procedure we employ to calculate the hydrodynamic forces and efficiency has already been discussed extensively (Borazjani and Sotiropoulos, 2008). Therefore, only a brief description is given below for the sake of completeness.

In our simulations, the fish swims steadily along the positive x_3 direction. The component of the instantaneous hydrodynamic force along the x_3 direction (which, for simplicity, will be denoted as F) can be readily computed by integrating the pressure and viscous forces acting on the body as follows (where repeated indices imply summation):

$$F(t) = \int_A (-pn_3 dA + \tau_{3j} n_j) dA, \quad (6)$$

where n_j is the j^{th} component of the unit normal vector on dA , and τ_{ij} is the viscous stress tensor. The non-dimensional force coefficient (C_F) in the axial direction is defined as follows:

$$C_F = \frac{F(t)}{\rho U^2 L}, \quad (7)$$

where ρ is the density of the fluid.

Depending on whether $F(t)$ is negative or positive, it could contribute to either hydrodynamic drag, $D(t)$, or thrust, $T(t)$. To separate the two contributions, we adopt the force decomposition approach proposed by Borazjani and Sotiropoulos (Borazjani and Sotiropoulos, 2008):

$$T(t) = T_p + T_v = \frac{1}{2} \left(\int_A -pn_3 dA + \left| \int_A pn_3 dA \right| \right) + \frac{1}{2} \left(\int_A \tau_{3j} n_j dA + \left| \int_A \tau_{3j} n_j dA \right| \right), \quad (8)$$

$$-D(t) = -(D_p + D_v) = \frac{1}{2} \left(\int_A -pn_3 dA - \left| \int_A pn_3 dA \right| \right) + \frac{1}{2} \left(\int_A \tau_{3j} n_j dA - \left| \int_A \tau_{3j} n_j dA \right| \right), \quad (9)$$

where the subscripts p and v refer to force contributions from pressure and viscous terms, respectively.

The numerical details for calculating the various surface integrals involved in the above equations in the context of the HCIB numerical method can be found in Borazjani (Borazjani, 2008). A detailed validation study demonstrating the accuracy of our numerical approach for calculating the viscous and pressure components of the hydrodynamic force can be found in Borazjani (Borazjani, 2008) and Borazjani and Sotiropoulos (Borazjani and Sotiropoulos, 2008).

The power loss due to lateral undulations of the fish body is calculated as follows:

$$P_{side} = \int -pn_2 \dot{h} dA + \int \tau_{2j} n_j \dot{h} dA, \quad (10)$$

where, \dot{h} is the time derivative of the lateral displacement ($i=2$ direction), i.e. the velocity of the lateral undulations.

The Froude propulsive efficiency (η) based on the thrust force for constant speed inline swimming is defined as follows (see Tytell and Lauder, 2004):

$$\eta = \frac{\bar{T}U}{\bar{T}U + \bar{P}_{side}}, \quad (11)$$

where \bar{T} is the mean thrust force over the swimming cycle, U is the steady swimming speed, and \bar{P}_{side} is the mean power loss over the swimming cycle due to lateral undulations.

The Froude efficiency based on the elongated body theory (EBT) for steady swimming is given as follows (Lighthill, 1969):

$$\eta_{EBT} = \frac{1}{2}(1 + \beta), \quad (12)$$

where $\beta=U/V$ is the slip velocity, defined as the ratio of the swimming speed U to the speed V of the backward undulatory body wave. Cheng and Blickhan (Cheng and Blickhan, 1994) introduced an improved EBT efficiency formula (denoted herein as EBT-2) that takes into account the slope of the fish tail where all the mean quantities are computed:

$$\eta_{EBT-2} = \frac{1}{2}(1 + \beta) - \frac{1}{2}\alpha^2 \frac{\beta^2}{1 + \beta}. \quad (13)$$

In the above equation the quantity α is defined as:

$$\alpha = \frac{\lambda}{2\pi} \frac{h'(L)}{h(L)}, \quad (14)$$

where $h(L)$ is the undulation amplitude and $h'(L)$ is its derivative relative to x_3 (slope) at the tail (Cheng and Blickhan, 1994).

It is important to note that the Froude efficiency equation (Eqn 11) can only be applied under inline, constant-speed swimming when the thrust force is balanced exactly by the drag force, and the net force acting on the fish body is zero (Borazjani and Sotiropoulos, 2008). If this equilibrium condition is violated, the fish will either accelerate or decelerate, the velocity U will no longer be constant, and Eqn 11 is not meaningful. Therefore, the propulsive efficiency is only computed at the critical Strouhal number (St^*) for which the net force F acting on the fish body is zero, as in Borazjani and Sotiropoulos (Borazjani and Sotiropoulos, 2008).

RESULTS AND DISCUSSION

Strouhal number and Reynolds number effects

To systematically compare the effects of varying Re and St on the hydrodynamics of anguilliform swimming with the results we obtained for carangiform swimming, we carry out simulations at the same Reynolds numbers as in Borazjani and Sotiropoulos (Borazjani and Sotiropoulos, 2008). Viscous flow simulations are carried out for $Re=300$ and 4000 , and inviscid simulations are carried out to simulate the flow in the limit of $Re=\infty$. For $Re=300$ and 4000 , the Strouhal number is varied incrementally from zero (rigid body case) until the mean net force on the fish body becomes greater than zero (see below for details). For $Re=\infty$, simulations are carried out over a narrower range of Strouhal numbers centered around the value at which the net force on the fish crosses zero.

To begin our discussion, Fig. 3 shows the time history of the instantaneous hydrodynamic axial force coefficient C_F (see Eqn 7) as a function of Strouhal number for $Re=4000$ for both anguilliform and carangiform swimmers; in this and all subsequent figures where we include results for carangiform swimming, these results are from Borazjani and Sotiropoulos (Borazjani and Sotiropoulos, 2008). Recall that in our simulation the virtual swimmer cannot move and, thus, the net hydrodynamic force is absorbed by the hypothetical tether that holds the fish in place. In other words, the force shown in Fig. 3 is the net force that would be available to accelerate the fish either forward or backward (depending on its sign) at the instant when the hypothetical numerical tether is removed. Given the sign convention we introduced in the previous section, $C_F > 0$ when $T > D$, i.e. when the thrust force exceeds the drag force and the net force on the body is in the direction of the fish motion. To facilitate our discussion and as in Borazjani and Sotiropoulos (Borazjani and Sotiropoulos, 2008) we shall refer to this situation as the net force

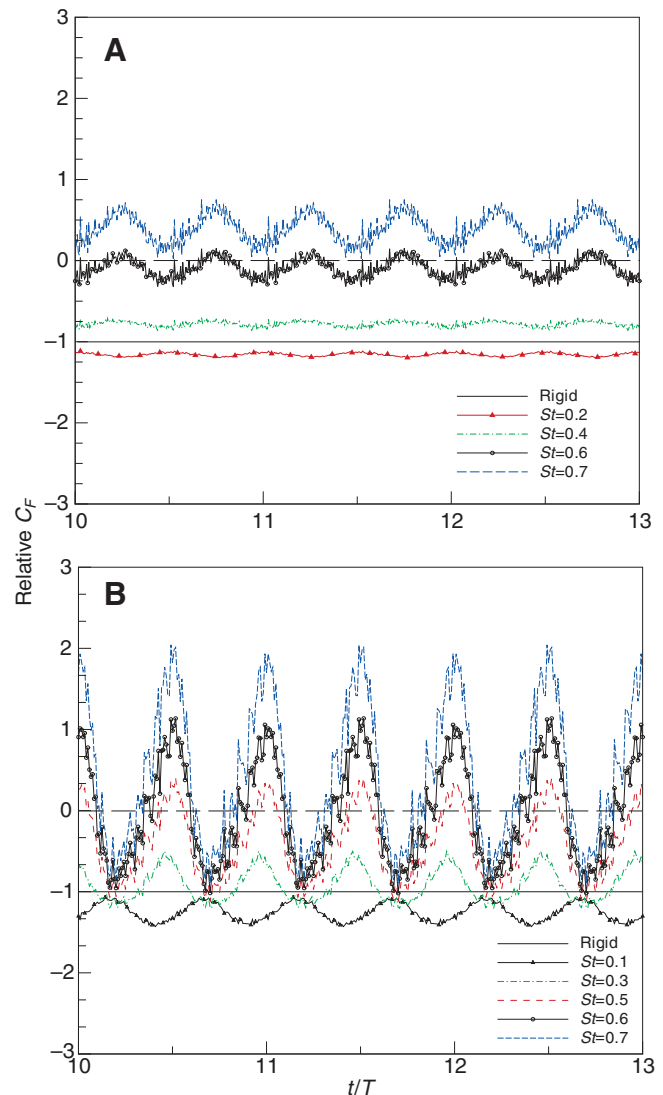


Fig. 3. Time history of the axial force coefficient (C_F) normalized by the rigid body drag coefficient for different St at $Re=4000$ of (A) the anguilliform virtual swimmer compared with (B) the carangiform virtual swimmer (Borazjani and Sotiropoulos, 2008). Positive and negative values indicate that the force is of thrust- and drag-type, respectively.

being of thrust type. Similarly, the situation with $C_F < 0$ will be referred to as the net force being of drag type. Such notation is used herein to characterize the direction of the net force and should not be confused with the terms thrust or drag force, which refer only to the thrust or drag portions of the instantaneous net force (see Eqns 8–9). The values of C_F in Fig. 3 and in all subsequently presented figures have been scaled with the axial force coefficient calculated for the rigid body fish ($St=0$) at the same Reynolds numbers. The line corresponding to the force acting on the rigid body $C_F=-1$ is marked in Fig. 3 to readily gauge the level of the net force for each St relative to the rigid body drag.

Fig. 3 reveals a number of important similarities and differences between the anguilliform and carangiform modes of aquatic swimming. With reference to our previous findings (Borazjani and Sotiropoulos, 2008), the following trends are shared by both modes of swimming:

(1) For all simulated St , the axial force coefficient in each cycle exhibits two peaks corresponding to the forward and backward tail strokes (Muller et al., 2001).

(2) As the Strouhal number increases from zero, the net force remains of drag type ($C_F < 0$) throughout the entire swimming cycle up to a threshold Strouhal number at which the first excursions into the thrust-type regime ($C_F > 0$) are observed.

(3) Further increase of the Strouhal number above the aforementioned threshold leads to longer and larger amplitude excursions into the thrust-type regime, ultimately yielding a positive mean net force. The Strouhal number at which this transition occurs is called the critical Strouhal number (St^*).

(4) For sufficiently small Strouhal numbers, $St < 0.3$, the undulations of the body cause a net force of drag type with a magnitude greater than the drag force of the rigid fish at the same Reynolds number. That is, low Strouhal number body undulations cause the magnitude of the drag-type net force to increase over that of the rigid body. For higher Strouhal numbers ($0.3 < St < St^*$), the undulations of the body cause a net force also of drag type but of lower magnitude than the corresponding rigid body net force. It is important to note that even though Fig. 3 shows results only for $Re=4000$, similar plots for $Re=300$ and ∞ (not shown) exhibit essentially all the above qualitative trends. The only quantitative difference among the various Reynolds numbers is the value of St^* at which the net force sign transition occurs. This issue will be revisited later in our discussion.

The above similarities notwithstanding, Fig. 3 also reveals an important difference between anguilliform and carangiform swimming. Namely, there is a profound difference in the amplitude of the fluctuations of the axial force coefficient above the respective mean value. It is evident from Fig. 3 that carangiform swimming is characterized by significantly higher (up to four times larger) fluctuation amplitudes above the mean than anguilliform swimming. To further analyze this important difference, Fig. 4 compares the time evolution of the axial force coefficient and its pressure and viscous components at $Re=4000$ and the respective St^* for the two modes of swimming. It is evident from this figure that for both swimming modes the fluctuations of the total force are primarily due to fluctuations in the pressure component of the force since the viscous contribution exhibits only very mild undulations about the mean. Carangiform swimmers, therefore, seem to exhibit significantly larger fluctuation amplitudes of the pressure force than anguilliform swimmers. To quantify this important aspect of undulatory swimming, in Fig. 5 we plot the root-mean-square (rms) of the axial force coefficient fluctuations normalized by the rigid body drag coefficient. It is evident from this figure that the rms

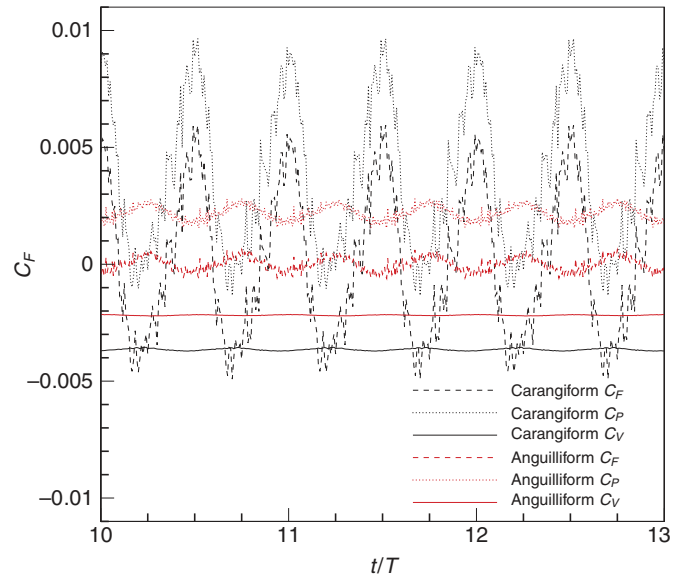


Fig. 4. Time history of the axial force coefficient (C_F , broken lines) and its pressure (C_P , dotted lines) and viscous (C_V , solid lines) components at $Re=4000$ and critical $St^*=0.62$ for the anguilliform virtual swimmer (in red) compared with the carangiform virtual swimmer at $St^*=0.6$ (in black) (Borazjani and Sotiropoulos, 2008). Positive and negative values indicate that the force is of thrust- and drag-type, respectively.

values for the carangiform swimmer are much larger than the corresponding values for the anguilliform swimmer. Furthermore, it is also observed that as St and Re increase the intensity of the force fluctuations also tends to increase for both swimmers.

The difference in the intensity of force fluctuations between the two modes of swimming points to the conclusion that, at the limit of constant-speed, inline-swimming, anguilliform swimmers should be able to swim smoother than carangiform swimmers exhibiting significantly less velocity fluctuations. This conclusion is in fact in agreement with experimental observations. Observations of swimming eels (anguilliform) have revealed about 10% velocity fluctuations about the mean velocity U (Muller et al., 2001) while swimming mullets (carangiform) have been found to exhibit velocity fluctuations more than 23% of the mean (Muller et al., 1997).

As we reported previously (Borazjani and Sotiropoulos, 2008) for carangiform swimming, St^* is also a function of the Reynolds number for anguilliform swimming. To illustrate this dependence, in Fig. 6 we plot the variation of the mean net axial force coefficient, \bar{C}_F (averaged over several swimming cycles and scaled by the corresponding value for the rigid body at the same Reynolds number), with St for all three simulated Reynolds numbers. Comparing the results in Fig. 6 with those reported in Fig. 4 in Borazjani and Sotiropoulos (Borazjani and Sotiropoulos, 2008) for carangiform swimming, the following observations can be made.

For both swimming modes at low St numbers, the mean net force is of drag type, and its magnitude initially increases relative to that of the rigid body for both $Re=300$ and 4000.

As St is increased, the mean net force, while remaining of drag type, is gradually diminishing in magnitude and ultimately its magnitude becomes smaller than that acting on the rigid body. The Strouhal number at which this transition occurs appears to be the same for both Reynolds numbers but different for the two swimming modes ($St=0.25$ and 0.3 for carangiform and anguilliform swimmers, respectively).

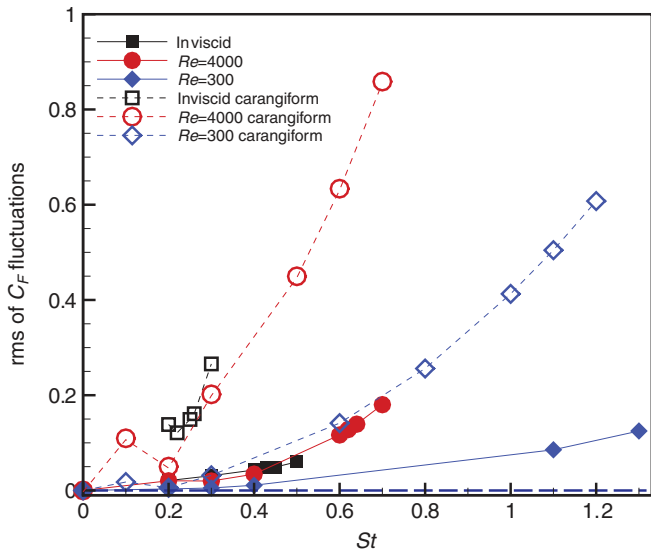


Fig. 5. Comparison of root-mean-square (rms) of axial force coefficient (C_F) fluctuations normalized by the rigid body drag coefficient for the virtual anguilliform swimmer (filled symbols) and the carangiform swimmer (open symbols).

As the St is further increased above a critical threshold (St^*), the force becomes positive in the mean, which marks the transition from a mean net force of drag type to a mean net force of thrust type. As in carangiform swimming, St^* is a decreasing function of Reynolds number: $St^*=1.3, 0.62$ and 0.45 for $Re=300, 4000$ and ∞ , respectively, for anguilliform swimming while $St^*=1.08, 0.6$ and 0.26 for $Re=300, 4000$ and ∞ , respectively, for carangiform swimming.

St^* approaches the range of Strouhal numbers at which most anguilliform swimmers swim in nature ($St \sim 0.3-0.5$) (Fish and Lauder, 2006; Muller et al., 2008) for $Re > 4000$.

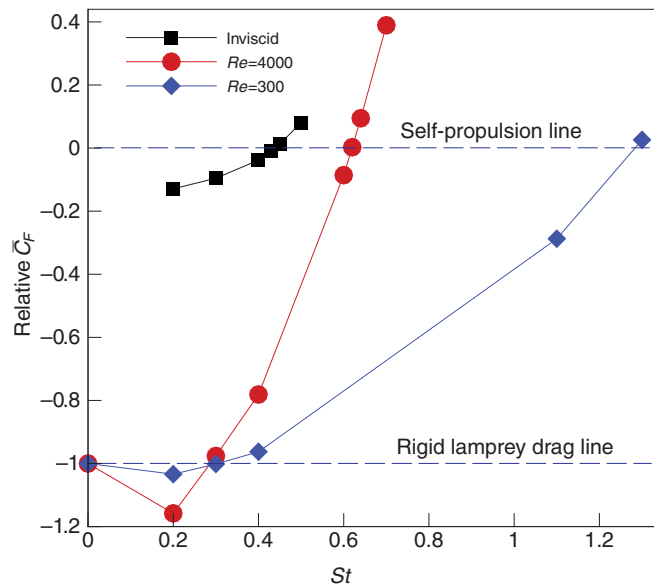


Fig. 6. Effect of Reynolds and Strouhal numbers on the mean axial force coefficient (C_F) produced by the tethered lamprey. The axial force coefficient is time-averaged and normalized by the rigid body drag coefficient. The lower broken horizontal line shows the rigid body drag coefficient, and the upper broken horizontal line shows the zero mean axial force coefficient, i.e. self-propulsion limit.

Similar to carangiform swimming, for each Re there is a unique St^* at which steady inline swimming is possible for the anguilliform swimmer. This finding confirms our previous assertion (Borazjani and Sotiropoulos, 2008) that, in addition to efficiency considerations (Triantafyllou and Triantafyllou, 1995; Triantafyllou et al., 2000), for a given Reynolds number fishes select the St at which they will undulate their body because this is the only Strouhal number at which they can produce enough thrust to cancel the drag they generate to swim steadily.

Effect of amplitude envelope on \bar{C}_F

It is well known that some fish vary their tail-beat amplitude as they accelerate. Bainbridge states that at low tail-beat frequencies (3–5 Hz) the amplitude increases with frequency and speed for three different fishes; namely dace, trout and goldfish (Bainbridge, 1958). Tytell reports that frequency, wave speed and tail-tip velocity increase significantly with increasing swimming speed while tail-beat amplitude increases only slightly (Tytell, 2004). Donley and Dickson report that the tail-beat amplitude increases with speed in chub mackerel but not in kawakawa tuna (Donley and Dickson, 2000). For eels, different tail-beat amplitude has been reported, e.g. $0.09-0.1L$ (Muller et al., 2001), $0.089L$ (Hultmark et al., 2007) and $0.069L$ (Tytell and Lauder, 2004). In our previous work for carangiform swimmers (Borazjani and Sotiropoulos, 2008) we did not investigate this effect as we kept the tail-beat amplitude constant. Here we explore the effect of this parameter for the anguilliform virtual swimmer.

As discussed previously, there are four parameters in fishlike swimming: Re, St, λ and $a(z)/L$. We keep all the non-dimensional parameters constant and only change the amplitude envelope by increasing a_{max} to $0.1L$ from $0.089L$. Fig. 7 shows the effect of the amplitude envelope increase on the mean axial force coefficient \bar{C}_F . It can be observed that for the low Re case ($Re=300$), the overall effect is very small and the \bar{C}_F for the larger a_{max} is only slightly reduced at the same Strouhal number. For the higher Re case

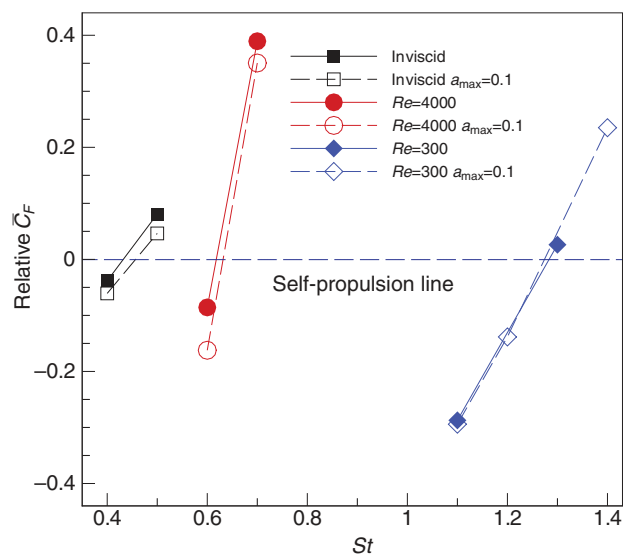


Fig. 7. Effect of the amplitude envelope $a(z)$ at different Reynolds and Strouhal numbers on the mean axial force coefficient produced by the tethered lamprey. The axial force coefficient is time-averaged and normalized by the rigid body drag coefficient. The broken horizontal line shows the zero mean axial force coefficient, i.e. self-propulsion limit.

($Re=4000$ and inviscid), however, the value of C_F for $a_{max}=0.1$ is less than the usual C_F at the same St by a larger margin. Remember that in order to keep the St constant while increasing the a_{max} , the tail-beat frequency f should decrease. It appears that at a higher Re , frequency is more important than amplitude in generating thrust due to the dominant role of inertial forces. However, at lower Re , where inertial forces are less important, the effect of f (or time period) becomes less significant.

Swimming efficiency

As already discussed above and in our previous work (Borazjani and Sotiropoulos, 2008), Eqn 11 is meaningful to calculate the Froude efficiency only at St^* , when the assumption of constant swimming speed is valid. In Table 1, the so-computed Froude efficiency is given for different Reynolds numbers at the corresponding value of St^* using the EBT (Eqn 12), EBT-2 (Eqn 13) and direct (CFD) calculation (Eqn 11) for both carangiform and anguilliform swimmers.

A striking new finding that follows from Table 1 is that, unlike carangiform swimmers for which the Froude efficiency is a monotonic function of Re and is maximized at $Re=\infty$, for anguilliform swimmers the efficiency calculated by the CFD method is maximized somewhere in the transitional regime. As seen in Table 1, the efficiency increases from $Re=300$ to 4000 and then decreases at $Re=\infty$. Note that the two EBT methods cannot capture the apparent peak at lower Re since they are inviscid methods and thus inherently not applicable to the transitional flow regime in which viscous forces are still significant.

Comparing the two modes of swimming, it is observed that the carangiform swimmer has a higher efficiency at $Re=\infty$ while the anguilliform swimmer has a higher efficiency at $Re=4000$. Both carangiform and anguilliform swimmers are very inefficient at low Re ($Re=300$) with similar Froude efficiency of about 18%. To the best of our knowledge, this is the first time that the effects of scale (Re) on propulsive efficiency are so clearly demonstrated for different modes of swimming.

The decrease in Froude efficiency for the anguilliform swimmer in the inviscid environment can be readily explained by the fact that anguilliform swimmers propel themselves as an undulatory pump (Muller et al., 2001); i.e. each part of the body generates thrust by accelerating the adjacent fluid. To demonstrate this more clearly, Fig. 8 shows a diagram with the force balance on an infinitesimal element of an undulating pump with a traveling wave velocity V and swimming velocity U . The element ‘sees’ an effective flow

Table 1. Calculated Froude efficiency percentages

Re	Carangiform			Anguilliform		
	EBT	EBT-2	CFD	EBT	EBT-2	CFD
300	59.5	59.3	18.86	60.69	60.67	17.62
4000	67.25	66.67	22.95	72.41	72.35	31.62
∞	92	89.47	47.55	80.88	80.78	18.89

Re, Reynolds number; EBT, elongated body theory; EBT-2, corrected elongated body theory; CFD, computational fluid dynamics.

velocity $\vec{U}^R = \vec{U} - \vec{V}$ coming toward it, which can be decomposed into components normal (\vec{U}_n^R) and tangential (\vec{U}_t^R) to the element. Such local relative flow exerts hydrodynamic forces in the normal (F_n) and tangential (F_t) directions as shown in the figure. The components of F_n and F_t along the swimming direction, denoted as T_n and T_t , respectively, contribute to the net force T_{net} exerted on the infinitesimal element. In the inviscid environment, accelerating the adjacent fluid by viscous forces is not possible as the fluid slips over the fish body, i.e. $F_t = T_t = 0$, and as such the net thrust force is reduced. In the viscous environment, on the other hand, the adjacent fluid is accelerated by the swimmer’s body due to the no-slip condition, and the viscous shear force increases T_t , thus contributing to a larger T_{net} .

For carangiform swimmers, the body undulations are concentrated in their caudal fin area and, as such, they generate thrust *via* a drastically different, lift-based mechanism that is similar to that in heaving and pitching foils. Let us illustrate the thrust generation for carangiform swimmers by treating the caudal fin as a foil moving with swimming velocity U in the horizontal direction while undulating with velocity U_{tail} in the vertical direction as shown in Fig. 9. The flow velocity relative to the foil is U_r and makes an angle with the foil cord. Therefore, the foil experiences both drag and lift forces, F_D and F_L , respectively. Both F_D and F_L have components in the swimming direction, denoted as T_D and T_L , respectively. As seen in Fig. 9, the lift generated thrust T_L acts to increase the net thrust force T_{net} while the drag-generated thrust T_D reduces it. In the inviscid environment, friction drag is zero, which reduces the drag force and causes the net force to increase. A more detailed discussion of these heuristic, albeit insightful, arguments that provide a qualitative explanation for the higher efficiency of carangiform swimmers relative to anguilliform swimmers at $Re=\infty$ can be found in Borazjani (Borazjani, 2008).

Power requirements of undulatory swimming

In this section we employ the results of our simulations to calculate the power requirement of undulatory swimming and compare the results with the power requirement of towing the rigid fish at the

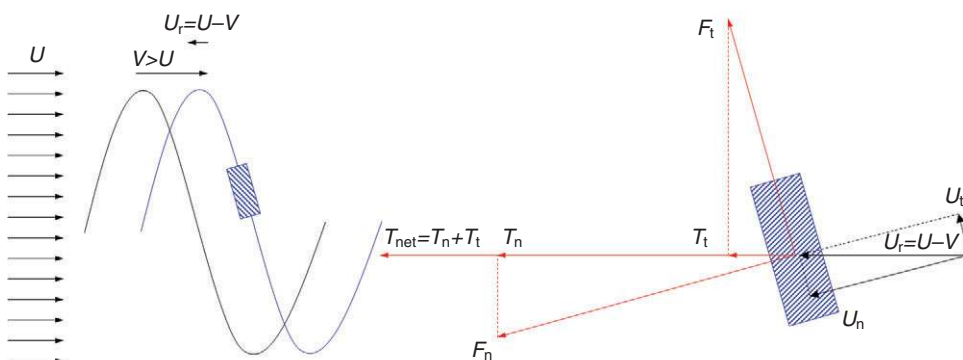


Fig. 8. Schematic showing anguilliform propulsion as an undulatory pump. U , swimming velocity; V , traveling wave speed; U_r is the relative velocity as observed from the shown element (shaded in blue); U_n , component of relative velocity in the normal direction; U_t , component of relative velocity in the tangential direction; F_n , normal force; F_t , tangential force; T_n , part of normal force in the direction of swimming; T_t , part of tangential force in the direction of swimming; T_{net} , net force in the direction of swimming.

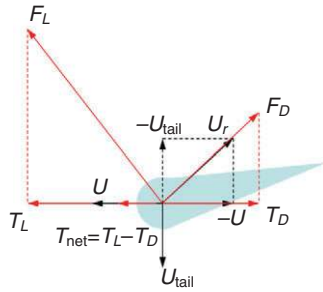


Fig. 9. Schematic showing carangiform propulsion as a heaving and pitching foil. U , swimming velocity; U_{tail} , the lateral velocity of the tail; U_r , relative velocity; F_L , lift force; F_D , drag force; T_L , part of the lift force in the direction of swimming; T_D , part of the drag force in the direction of swimming; T_{net} , net force in the direction of swimming.

same speed. At St^* , the mean axial power is zero since the mean axial force per cycle is zero. Therefore, the total power required at St^* is only the side power calculated by Eqn 10. The power requirement for the rigid fish to be towed at velocity U is simply the drag force multiplied by the velocity U . The power requirement has been calculated and non-dimensionalized by the factor $\rho U^3 L^2$, and the values are reported in Table 2.

The results in Table 2 clearly show that the power required by both anguilliform and carangiform swimmers decreases as Re increases. This trend was also observed experimentally for trout swimming by Tytell, who reported that the wasted power estimate decreases with swimming speed, at least for the few swimming speeds for which experimental data are available (Tytell, 2007). However, Tytell also reported that the eel's wasted power does not vary appreciably with swimming speed (Tytell, 2007). It is important to note, however, that Tytell cautioned about deriving firm conclusions from relatively few experimental measurements that are not adequate to distinguish in a statistically meaningful manner real differences among species from random variability among individuals.

In conjunction with the conclusions reached in the previous section in terms of the Froude efficiency, the swimming power calculations presented in Table 2 do show that, as Re is increased, carangiform swimming not only becomes more efficient but also requires less power for propulsion (Borazjani and Sotiropoulos, 2008). For anguilliform swimmers, on the other hand, the swimming power decreases as Re increases but, as already discussed in a previous section, the thrust force also decreases with increasing Re . The lower thrust force causes the Froude efficiency to decrease, thus making the anguilliform mode of BCF swimming less efficient at higher swimming speeds.

The results in Table 2 further show that, at a given Re , anguilliform swimmers need less power than carangiform swimmers, which is very much consistent with the experimental wasted power estimates

provided by Tytell (Tytell, 2007). If the power requirement, rather than the Froude efficiency, is used as a measure of swimming efficiency, as recommended by Schultz and Webb (Schultz and Webb, 2002), then our results show that the anguilliform swimmers are more efficient than carangiform swimmers. This striking finding could be due to either the morphology of the fish body or the specific BCF kinematics. In order to explore this very important question, we are currently carrying out self-propelled simulations with the mackerel and lamprey bodies each swimming with both kinematics (i.e. a mackerel will be made to swim both as a mackerel and an eel!). The results of these simulations, which we hope will settle this major issue, are beyond the scope of this work and will be presented in a future communication.

Table 2 also shows that, for a given Re , the power requirement of undulatory swimming is higher than that required to tow the rigid fish at the same speed both for the anguilliform and carangiform swimmers. As previously discussed (Borazjani and Sotiropoulos, 2008), all the kinematic and computational models to date have shown the same trend (for a review, see Schultz and Webb, 2002). However, this finding is in contrast with the results of Barrett et al. (Barrett et al., 1999), who showed through experimental measurements with a robotic fish that the power required for the tethered fish to move at constant speed U with undulatory body motion is less than that for the rigid body. It is important to point out, however, that whether body undulations increase or decrease the power required for swimming at all Re cannot be conclusively resolved by our work, and simulations at much higher Re will be required for definitive conclusions – see Borazjani and Sotiropoulos (Borazjani and Sotiropoulos, 2008) for a more detailed discussion.

Finally, it is worth mentioning here that some of the numerical values we present in Table 2 are reasonably close to the experimental values of wasted power reported by Tytell (Tytell, 2007). In Table 2, we non-dimensionalized the power by $\rho U^3 L^2$, while Tytell scaled his power estimate values by $\frac{1}{2} \rho U^3 S$, where S is the fish surface area: $0.18L^2$ for eel, $0.54L^2$ for trout and $0.69L^2$ for bluegill. Upon non-dimensionalizing our calculated power coefficients at $Re=\infty$ using Tytell's approach (Tytell, 2007), and assuming that the S values for eel and trout are good estimates for a lamprey and a mackerel, respectively, we obtain side-power coefficient values of 0.002 for the anguilliform swimmer (lamprey) and 0.0015 for the carangiform (mackerel) swimmer. The calculated value for the anguilliform swimmer is strikingly close to the corresponding value of 0.004 reported by Tytell for eel (Tytell, 2007). The computed value for the mackerel swimmer, on the other hand, is of the same order of magnitude as the 0.007 value reported by Tytell for trout but the larger discrepancy in this case could, at least in part, be due to the fact that we have assumed that the surface area S of the trout is a good approximation to that for the mackerel. Even though, and as we already mentioned above, the experimental values reported in Tytell's work (Tytell, 2007) are too few to obtain statistically meaningful wasted power estimates representative of various species, the reasonable agreement between our simulations and the experimental values is certainly encouraging and noteworthy.

Table 2. Calculated power requirements

Re	Carangiform		Anguilliform	
	P_{rigid}	P_{Sr}	P_{rigid}	P_{Sr}
300	2.6165×10^{-2}	1.4157×10^{-1}	1.5219×10^{-2}	1.1269×10^{-1}
4000	4.8921×10^{-3}	1.3671×10^{-2}	2.3710×10^{-3}	4.7265×10^{-3}
Inviscid	0	3.9598×10^{-4}	0	2.1296×10^{-4}

Re , Reynolds number; P_{rigid} , power coefficient for towing the rigid fish body; P_{Sr} , power coefficient at critical St^* .

Is undulatory locomotion drag-reducing or drag-increasing?

As discussed extensively in Borazjani and Sotiropoulos (Borazjani and Sotiropoulos, 2008), some previous work indicated that undulatory motion is drag increasing (Lighthill, 1971; Fish et al., 1988; Fish, 1993; Liu and Kawachi, 1999; Anderson et al., 2001), while Barrett et al. concluded it is drag reducing (Barrett et al., 1999). We previously reconciled these conflicting results for carangiform swimmers by decomposing the net force into drag and thrust

components as in Eqns 8 and 9 and decomposing the total drag into friction and form drag as in eqn 7 of Borazjani and Sotiropoulos (Borazjani and Sotiropoulos, 2008). The major trends revealed in Borazjani and Sotiropoulos (Borazjani and Sotiropoulos, 2008) are also observed for anguilliform swimmers, as shown in Fig. 10, which depicts the total, form and friction drag forces normalized by the rigid body drag for the anguilliform case. These similarities are discussed below with reference to fig. 5 of Borazjani and Sotiropoulos (Borazjani and Sotiropoulos, 2008) for the carangiform results.

For both Reynolds numbers and swimming modes, the total drag force initially increases above that of the rigid body drag with the maximum at the lowest St and the overall increase level being higher for the higher Re . As St is increased further, the drag force starts to decrease, and at $St \approx 0.3$ it decreases below the rigid body drag for both Reynolds numbers. Beyond that point, however, a distinctly different behavior is observed for the two Re . For both anguilliform and carangiform swimmers at the lower Reynolds number ($Re=300$)

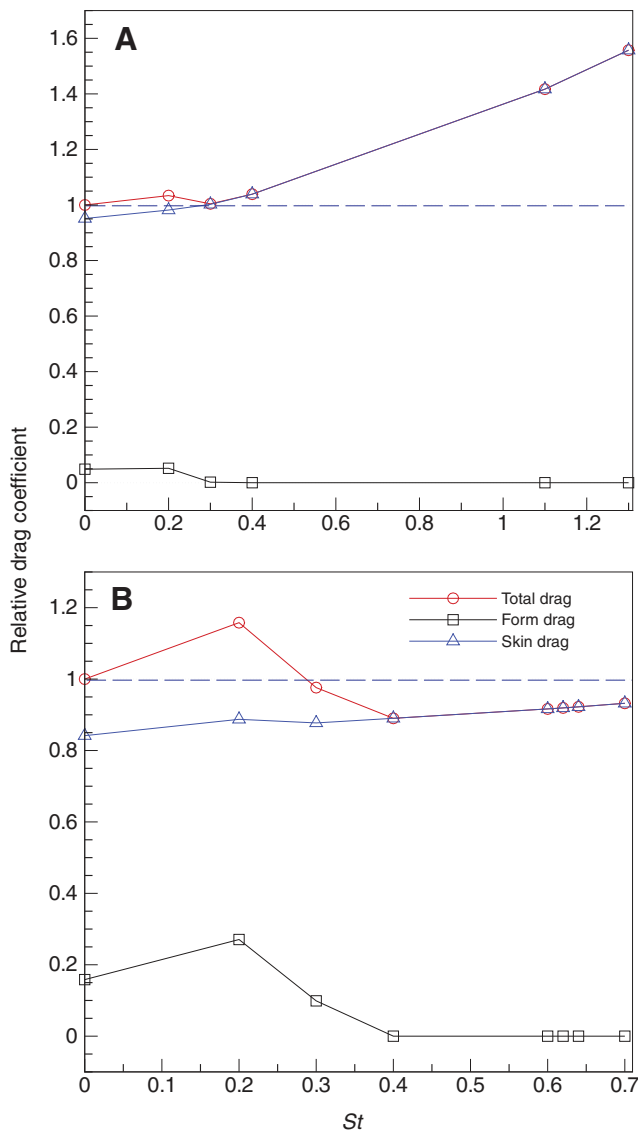


Fig. 10. Variation of the skin (friction) drag, form and total drag with Strouhal number at two Reynolds numbers: $Re=300$ (A) and $Re=4000$ (B). The drag forces are calculated using Eqn 9. All the drag coefficients are normalized by the rigid body drag coefficient.

and for $St > 0.3$ the drag starts increasing again above the rigid body threshold while for $Re=4000$ the drag is reduced monotonically, asymptoting toward an approximately constant value – approximately 75% and 90% of the rigid body drag at $St=0.6$ for carangiform and anguilliform, respectively.

In both carangiform and anguilliform swimming modes, the friction drag force increases monotonically with Strouhal number while the form drag initially increases and then decreases, asymptoting toward zero at about $St > 0.6$ for both Reynolds numbers. As one would anticipate, the friction drag is the major contributor to the total drag force at $Re=300$ and is responsible for the monotonic increase of the total drag force for $St > 0.3$. For $Re=4000$, the friction drag is higher than the form drag but varies only mildly with Strouhal number, increasing from 0.66 for the rigid body to an asymptotic limit of 0.75 for $St > 0.5$. Consequently, the variation of the total drag for this case is dominated by the non-monotone variation of the form drag, which, as mentioned above, initially increases at the lowest St and then asymptotes to zero for $St > 0.6$.

The above results for anguilliform swimmers reinforce our previous findings (Borazjani and Sotiropoulos, 2008) and show that, independent of the swimming mode and fish morphology, undulatory swimming increases the friction drag, which is the major contributor to the total drag at low Re . However, at high enough Re (e.g. $Re=4000$), the importance of viscous stresses diminishes, the friction drag tends to become fairly insensitive to the Strouhal number, and the variation of the total drag mimics essentially that of the form drag, which is reduced by the undulatory motion. It is, of course, important to note that the reduction in the form drag at higher St is not for free. As we have already pointed out (Borazjani and Sotiropoulos, 2008), the fish has to beat its tail faster to achieve drag reduction at higher St and thus needs to expend more power to accomplish this.

The physical mechanism that leads to the observed reduction in form drag in anguilliform swimming turns out to be exactly the same as in carangiform swimming and is governed by the ratio of the undulatory wave phase velocity V to the swimming speed U (Borazjani and Sotiropoulos, 2008). We show this in Fig. 11 by plotting instantaneous streamlines and pressure contours at the mid-plane of the anguilliform swimmer in the frame of reference moving with the undulatory wave phase velocity V for $Re=4000$ and $St=0$ (rigid body), 0.2 ($U/V=1.39$) and 0.4 ($U/V=0.69$). Note that the moving frame of reference is selected because, in the case of a swimming fish, flow separation occurs relative to the undulating body and can only be visualized clearly in the frame of reference that moves with the body wave velocity V – see Shen et al. (Shen et al., 2003) for a detailed discussion of this issue. As seen from Fig. 11A, the flow around the rigid body ($St=0$) does not separate as one would anticipate given the highly streamlined and slender body shape. As the body begins to undulate, however, and as long as V is less than U , the flow separates at the posterior of the body (see results in Fig. 11B for $St=0.2$) because the undulatory body wave is such that it acts to retard the near-wall flow relative to the free stream. The onset of separation explains the initial increase of the form drag force relative to the rigid body drag observed in Fig. 10. At St sufficiently high for the condition $V > U$ to be satisfied ($St > 0.28$ in our case), separation is eliminated (see Fig. 11C for $St=0.4$) and the drag force is reduced below that of the rigid body drag at the same Re . In this case, the motion of the undulating fish body is piston-like and acts to accelerate the slower moving ambient fluid, thus creating a positive (stagnation) pressure region at the posterior portion of the fish body, which reduces the form drag – this is clearly evident in the pressure contours shown in Fig. 11C. This argument

is entirely consistent with the results previously shown in Fig. 10, which reveal that for the viscous flow simulations the drag force is first reduced below that of the rigid body for $St > 0.3$. This Strouhal number is very close to the $St = 0.28$ value above which the condition $V > U$ is satisfied for the anguilliform swimmer.

Three-dimensional wake structure

The wake of aquatic swimmers has been studied extensively in the laboratory both for carangiform (Muller et al., 1997; Wolfgang et al., 1999; Nauen and Lauder, 2002) and anguilliform (Muller et al., 2001; Tytell and Lauder, 2004; Hultmark et al., 2007) swimmers using the PIV technique. These experiments showed that the

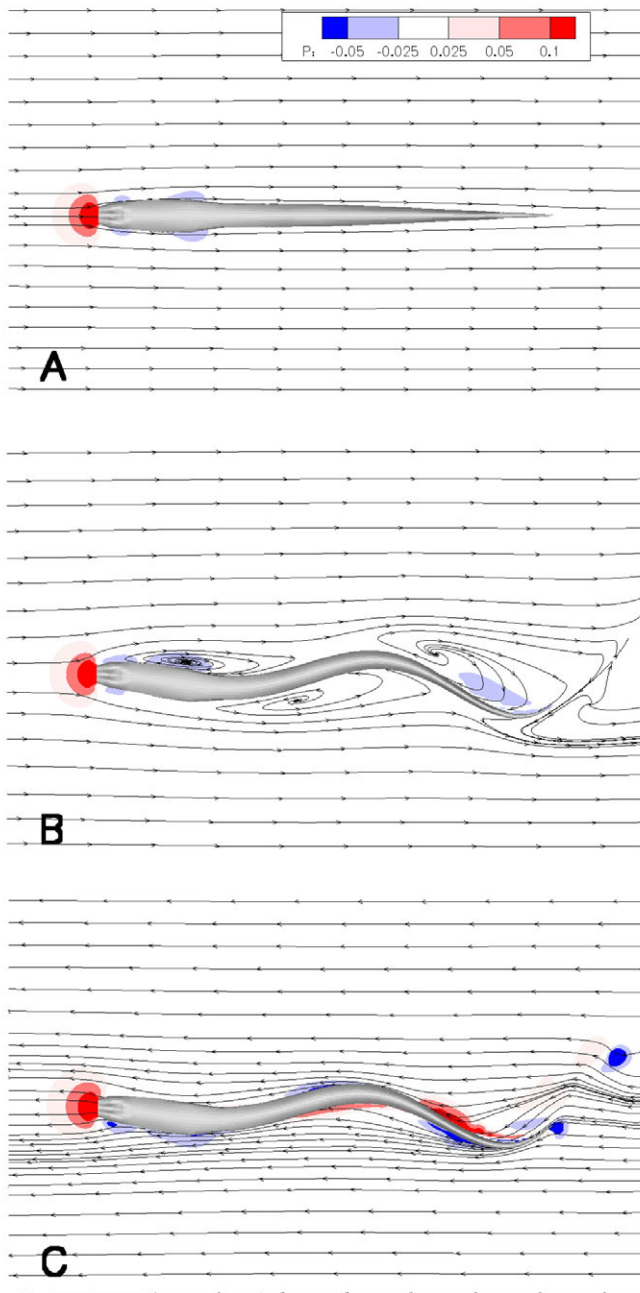


Fig. 11. Pressure contours and streamlines in mid-plane of the fish relative to a frame moving with the body traveling wave speed V ($Re = 4000$). (A) Flow does not separate for the straight rigid fish. (B) Flow separates for $St = 0.2$, $U/V = 1.39$. (C) Flow does not separate for $St = 0.4$, $U/V = 0.69$.

vortices in the wake of free-swimming anguilliform fishes organize in two distinct rows with two vortices shed per tail-beat such that discrete jets are formed between each vortex pair with force components in the downstream (thrust) and lateral directions (Muller et al., 2001; Tytell and Lauder, 2004; Hultmark et al., 2007) (see Fig. 12B). By contrast, the vortices in the wake of free-swimming carangiform fishes organize in a single row such that a continuous jet flow is formed between the vortices, which has been dubbed a reverse Karman street (Rosen, 1959) (see Fig. 12A).

In our previous simulations for the tethered carangiform swimmer, we found a reverse Karman street wake consisting of a single row of vortices for the inviscid, constant swimming speed case ($St^* = 0.26$), which is the case that corresponds closer (both in terms of Re and St) to the data available in the literature experiments with live carangiform swimmers (Borazjani and Sotiropoulos, 2008). On the other hand, for the tethered anguilliform swimmer, we find a double row of vortices for the constant swimming speed, inviscid flow case ($St^* = 0.45$), which is also the case that corresponds closer to the data available in the literature experiments with live anguilliform swimmers. This is shown in Fig. 13, in which we plot the simulated near-wake velocity and vorticity fields in the horizontal symmetry plane of the anguilliform swimmer at $Re = \infty$ and $St = 0.45$. The computed results are very similar to experimental measurements for a freely swimming eel obtained using PIV – see figs 3 and 6 of Muller et al. (Muller et al., 2001), fig. 5 of Tytell and Lauder (Tytell and Lauder, 2004) and fig. 6 of Hultmark et al. (Hultmark et al., 2007).

Our simulations have also revealed different wake patterns depending on Re and St , as shown in Fig. 14, which depicts three such representative wake patterns for the anguilliform swimmer. To facilitate the classification of the various wake patterns observed in our simulations we use the wake characterization convention we introduced in Borazjani and Sotiropoulos (Borazjani and Sotiropoulos, 2008): (1) depending on the direction of the common flow between the wake vortices the wake can be characterized as being of thrust or drag type and (2) depending on the layout of the vortical structures the wake can be characterized as consisting of single or double row vortices (Koochesfahani, 1989).

For the carangiform swimmer a single row wake can be either of drag or thrust type, as previously shown in fig. 8A and fig. 8B, respectively, of Borazjani and Sotiropoulos (Borazjani and Sotiropoulos, 2008). For the anguilliform swimmer, however, only the drag-type single row wake structure was observed in the range of simulated Re and St numbers, as shown in Fig. 14A. The main

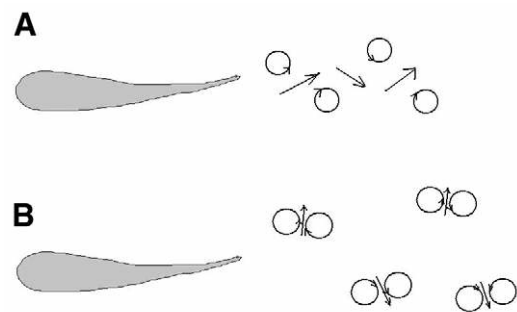


Fig. 12. Sketch of the wake behind a steady undulatory swimmer. (A) A single row of vortices observed behind carangiform swimmers. (B) A double row of vortices observed behind anguilliform swimmers. The circles indicate the shed vortices, with the arrowheads indicating their rotational sense. The arrows indicate the jet flows.

characteristic of the single-row wake pattern is that it remains confined within a relatively narrow parallel strip that is centered on the axis of the fish body and consists of Karman-street-like vortices. A double-row anguilliform wake that is of thrust type is shown in

Fig. 14B ($Re=\infty, St=0.45$). This wake pattern is distinctly different from the single-row wake as it is characterized by the lateral divergence and spreading of the vortices away from the body in a wedge-like arrangement.

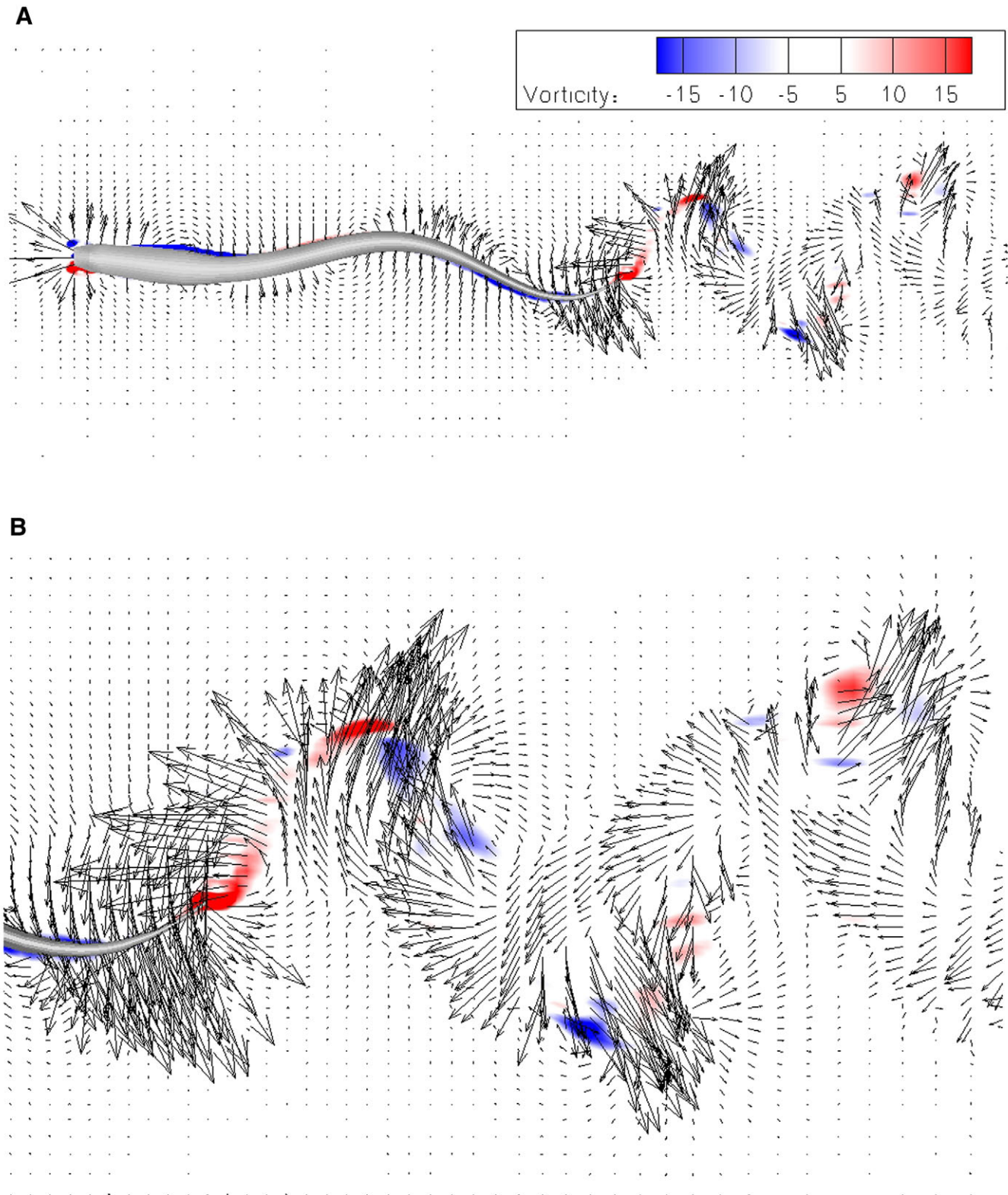


Fig. 13. Calculated out-of-plane vorticity contours with velocity vectors for the anguilliform swimmer at $Re=\infty, St=0.45$ on the horizontal (x_1-x_3) mid-plane. For clarity, only every third velocity vector is plotted.

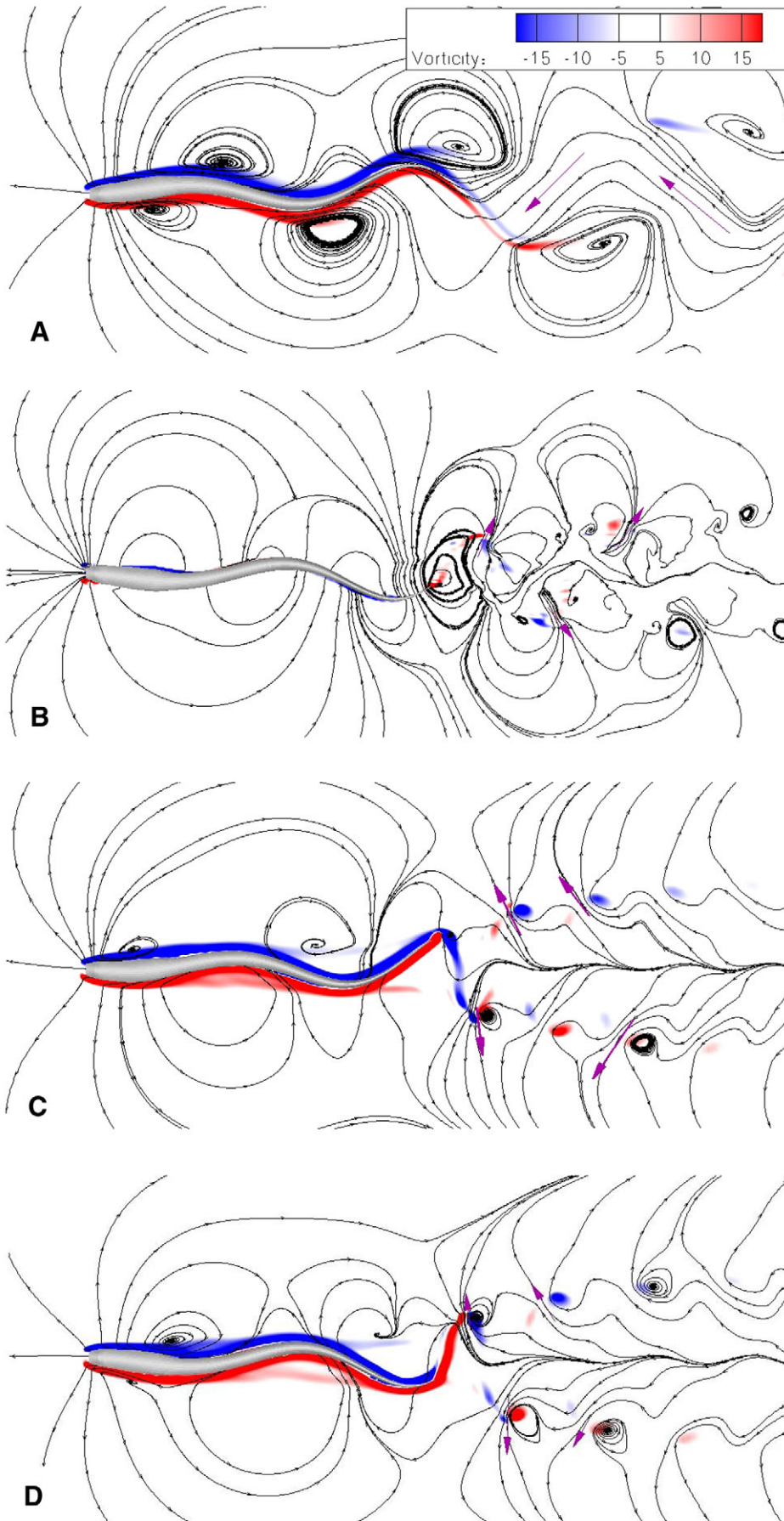


Fig. 14. Instantaneous streamlines with vorticity contours for anguilliform swimmer showing: (A) a single-row regular Karman street ($Re=4000$, $St=0.2$, $C_F=0.0027$); (B) a double-row thrust-type wake ($Re=\infty$, $St=0.45$, $C_F=3\times 10^{-5}$); (C) a double-row drag-type wake ($Re=4000$, $St=0.7$, $C_F=0.0009$); and (D) a double-row drag-type wake ($Re=4000$, $St=0.62$, $C_F=6\times 10^{-6}$). The red arrows show the general direction of the wake flow.

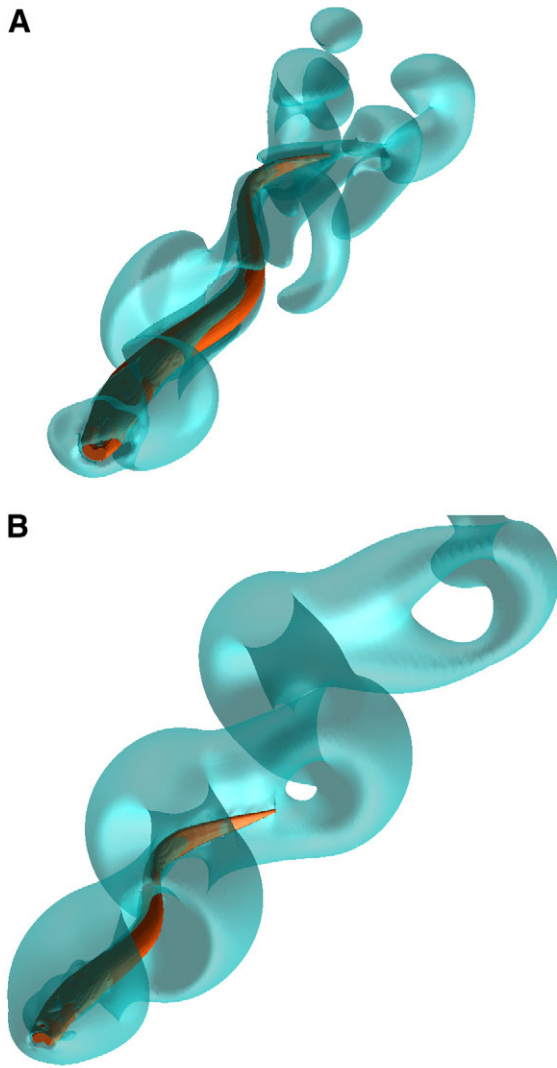


Fig. 15. Three-dimensional (3-D) vortical structures visualized using the q -criterion showing 3-D wake structures simulated for the $Re=300$ case. (A) Double-row wake at $St=1.1$ ($C_f=-0.0043$); (B) single-row wake at $St=0.2$ ($C_f=-0.0157$).

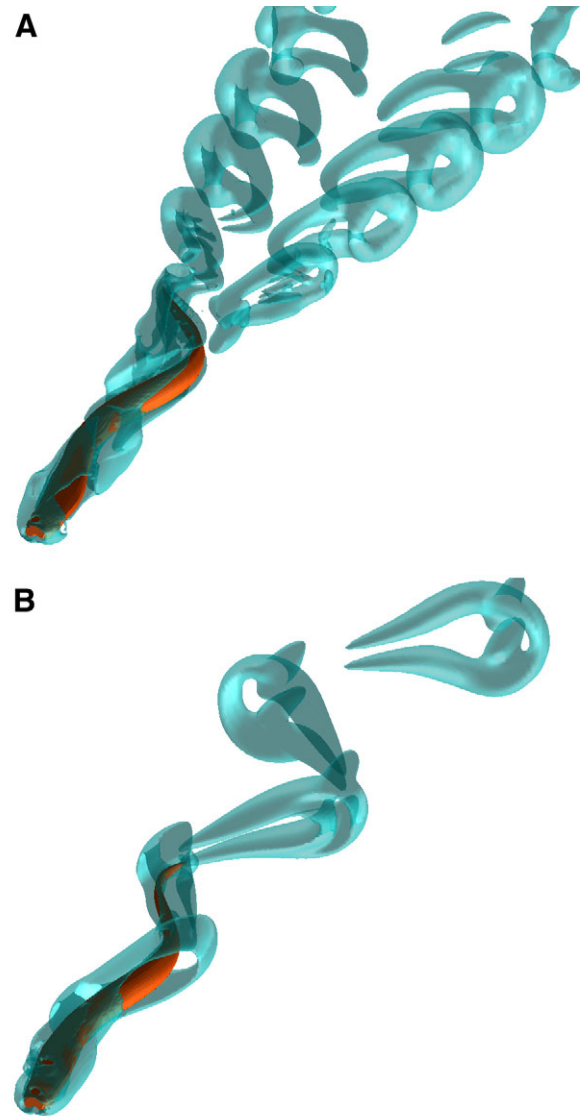


Fig. 16. Three-dimensional (3-D) vortical structures visualized using the q -criterion showing 3-D wake structures simulated for the $Re=4000$ case. (A) Double-row wake at $St=0.7$ ($C_f=0.0009$); (B) single-row wake at $St=0.2$ ($C_f=0.0027$).

Fig. 14C,D shows what appears to be from the 2-D standpoint drag-type wakes as the common flow between the vortex pairs in the wake is oriented in the lateral backward direction. It is important to note, however, that the net flux of the 3-D wake for this case is in fact of thrust type since, as shown in Fig. 6, at $Re=4000$ and $St=0.7$ the calculated mean axial force coefficient is positive and for $St=0.62$ is almost zero. This finding underscores the difficulties in assessing the wake type from velocity measurements at 2-D planes and confirms Dabiri's point that, in addition to the wake velocity field, a pressure-like term is also needed to correctly calculate the hydrodynamic forces (Dabiri, 2005).

Our results for anguilliform swimmers reinforce our previous finding for carangiform swimmers (Borazjani and Sotiropoulos, 2008) that for a fixed Reynolds number both the single- and double-row wake structures can emerge depending on the St number. Typically, at low St the single-row wake structure is observed (see Fig. 14A) while at high St the wake splits laterally and the double-row pattern emerges (Fig. 14B,C). As discussed previously

(Borazjani and Sotiropoulos, 2008), the dependence of the wake structure on the St number is to be expected since, by definition (see Eqn 2), the Strouhal number can be viewed as the ratio of the mean lateral tail velocity to the axial swimming velocity. Therefore, at high St , the vortices shed by the tail tend to have a larger lateral velocity component that advects them away from the centerline, causing them to spread in the lateral direction. Nevertheless, and as also discussed in Borazjani and Sotiropoulos (Borazjani and Sotiropoulos, 2008), the St at which the transition from the single- to the double-row wake structure occurs depends on the Reynolds number.

Although vorticity contours can provide significant insights into the wake structure, they are inherently 2-D and cannot comprehensively depict the 3-D structure of the flow. The 3-D wake structure for carangiform swimmers with a single vortex row wake structure has been suggested by Lighthill to consist of a series of connected vortex rings (Lighthill, 1969). For anguilliform swimmers, which exhibit a double vortex row wake, two disconnected vortex

rings have been hypothesized by Muller et al. (Muller et al., 2001). In our previous carangiform simulations we showed that, even though both 3-D wake patterns are found depending on the St , only at low Re was the 3-D wake structure as simple as was hypothesized to be in previous studies. Our simulations clearly showed that as the Reynolds number is increased the complexity of the vortical structures increases dramatically (Borazjani and Sotiropoulos, 2008).

In Figs 15–17, we visualize the 3-D structure of anguilliform wakes by plotting instantaneous iso-surfaces of the q -criterion (Hunt et al., 1988) for $Re=300$, 4000 and ∞ , respectively. The quantity q is defined as $q=\frac{1}{2}(\|\Omega\|^2-\|S\|^2)$, where S and Ω denote the symmetric and antisymmetric parts of the velocity gradient, respectively, and $\|\cdot\|$ is the Euclidean matrix norm. According to Hunt et al. (Hunt et al., 1988), regions where $q>0$ – i.e. regions where the rotation rate dominates the strain rate – are occupied by vortical structures. For each Re we show two St numbers corresponding to the single- and double-row vortex patterns.

Similar to carangiform swimmers, both wake types are also observed in the simulations for anguilliform swimmers depending on the St number. At low St , a single-row pattern emerges while at higher St the double-row structure is observed. Nevertheless, and as was the case for carangiform swimming, the rather simple wake structure that was hypothesized in previous experiments is observed only for the $Re=300$ case (Fig. 15), while for $Re=4000$ (see Fig. 16) the wake structure becomes significantly more complex. The single-row wake at $Re=300$ consists of braided hairpins whose heads and legs appear to have similar thickness. For the $Re=4000$ case, on the other hand, braided hairpins also form the single-row pattern, but in this case the hairpins have longer and more stretched legs and more slender heads. Note, however, that the smaller-scale vortical structures attaching to the hairpin vortices that started emerging in the wake of the carangiform swimmer [fig. 11B in Borazjani and Sotiropoulos (Borazjani and Sotiropoulos, 2008)] for the same set of governing parameters are not observed herein for the anguilliform swimmer (Fig. 16B).

For the double-row anguilliform wake, each vortex loop has two legs with slender ends, which are stretched to braid in the inside of the previous vortex loop in the same vortex row (Fig. 16A). The skeleton of this structure is very similar to the double-row structure obtained from the experiments with a pitching panel (Buchholz and Smits, 2008). By contrast, in the double-row carangiform wake [see fig. 11A in Borazjani and Sotiropoulos (Borazjani and Sotiropoulos, 2008)], each vortex loop is not as circular as in the anguilliform case and consists of very complex and highly 3-D coherent structures connected together through complex columnar vortices (Borazjani and Sotiropoulos, 2008). Finally, for both anguilliform and carangiform swimmers in the inviscid case, the single-row wake consists of connected vortex loops, which are flatter in shape and stretched in the streamwise direction (Fig. 17B). The double row, on the other hand, exhibits smaller structures than the $Re=4000$ case, and the complexity of the wake has increased further (Fig. 17A).

The above observations reinforce our previous conclusion for the carangiform case that the St is the main parameter governing the 3-D structure of the wake. Both types of wake structures have been observed, depending on St , for both anguilliform and carangiform virtual swimmers, which not only have different body morphology but also different swimming kinematics. This conclusion is also supported by the discussion in Muller et al. (Muller et al., 2008) and is consistent with what has been observed in nature: the

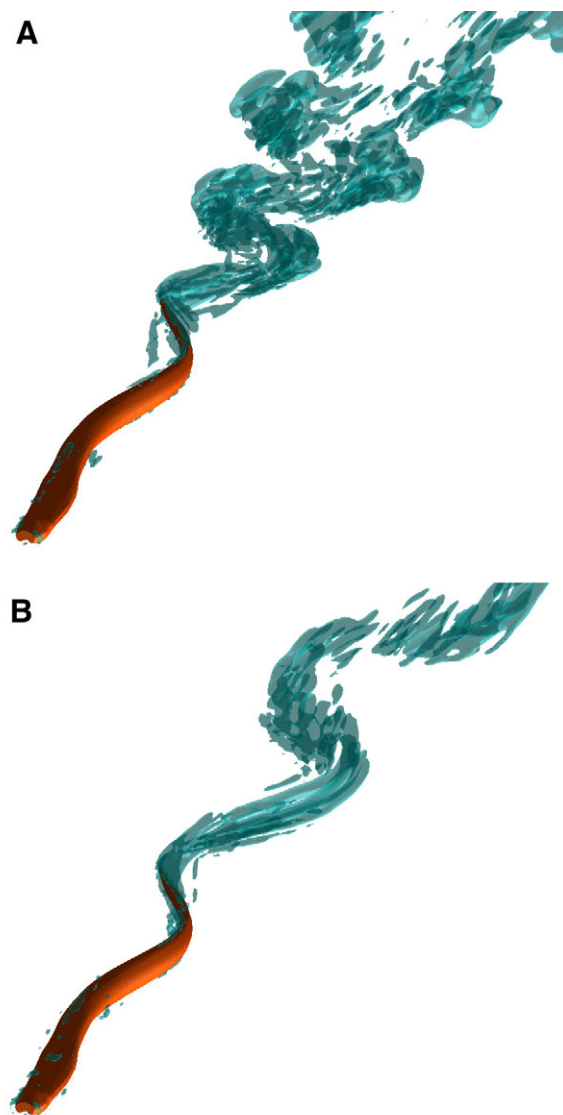


Fig. 17. Three-dimensional (3-D) vortical structures visualized using the q -criterion showing 3-D wake structures simulated for the inviscid case. (A) Double-row wake at $St=0.5$ ($C_f=0.0002$); (B) single-row wake at $St=0.2$ ($C_f=0.0003$).

anguilliform swimmers usually swim at higher St numbers (adult eel, 0.3–0.4; larval zebrafish, 0.35–2.0), where the double-row wake structure prevails, while the carangiform swimmers swim at lower St (0.2–0.35), where the single-row structure is found in our simulations.

Concluding remarks

In this companion paper to our previous work (Borazjani and Sotiropoulos, 2008), we constructed a virtual anguilliform swimmer and employed it to elucidate the hydrodynamics of this type of locomotion and compare it with carangiform swimming. The virtual tethered anguilliform swimmer allowed us to perform controlled numerical experiments under the same conditions as the carangiform swimmer (i.e. similar Reynolds and Strouhal numbers) and systematically compare the relative performance of these two modes of undulatory swimming. As such, we were able to pose and answer questions that cannot be tackled experimentally due to the inherent difficulties in performing and analyzing the results of

controlled experiments with live fish. The most important findings of our work are summarized as follows.

Anguilliform swimmers generate thrust more smoothly than carangiform swimmers in the sense that they exhibit net force fluctuations with significantly lower rms than carangiform swimmers. This finding explains why anguilliform swimmers are able to swim with less variation in their swimming velocity than carangiform swimmers, as observed in experiments with swimming eels.

The Froude efficiency of anguilliform swimmers has a peak within the transitional Re in stark contrast with carangiform swimmers, whose efficiency is maximized in the limit of $Re=\infty$.

Anguilliform swimmers are characterized by less power loss than carangiform swimmers at all simulated Re . However, for both swimmers the power loss decreases as Re is increased and, at all simulated Re , is higher than the power needed for towing the rigid fish at the same Re .

Increasing frequency while decreasing the tail-beat amplitude to keep St and all other parameters constant increases the axial force coefficient \bar{C}_F , particularly at higher Re (e.g. $Re>4000$). This suggests that the frequency of the undulations is more important than the amplitude in thrust generation.

Our simulations confirmed that many of our previous findings for carangiform swimming (Borazjani and Sotiropoulos, 2008) are also valid for anguilliform swimming, thus suggesting that there are several aspects of undulatory BCF locomotion that do not depend on the specific mode of swimming. These include the following:

(1) For a given Re , regardless of the swimming mode, there is a unique Strouhal number (St^*) at which body undulations produce sufficient thrust to exactly cancel the hydrodynamic drag, making constant-speed self-propulsion possible.

(2) St^* is a decreasing function of Re for both modes of swimming and reaches the range within which most fish swim in nature only at sufficiently high Re .

(3) Undulatory motion, regardless of its specific mode, is shown to increase the viscous drag as St increases. The form (pressure) drag, on the other hand, is shown to increase initially above the rigid body level at low St . At higher St , however, the form drag decreases below that of the rigid body for St values for which the phase velocity of the body undulatory wave exceeds the swimming speed ($V>U$). At low Re , the total drag mimics the viscous drag and increases with St . At sufficiently high Re , however, the variation of the total drag force mimics the form drag, which is effectively reduced by the undulatory motion.

(4) For $V>U$, separation in the posterior of the body is eliminated since the undulating body acts as a pump that tends to accelerate the outer flow. This trend is true for both swimming modes and is the reason why the form drag is reduced. For $V<U$, the flow separates from the fish body and increases the form drag above that of the rigid body drag. In such a case, the separation for the carangiform swimmer is restricted to the tail section but for the anguilliform swimmer it is observed even in the mid body area – compare Fig. 11B with fig. 6B of Borazjani and Sotiropoulos (Borazjani and Sotiropoulos, 2008).

(5) The 3-D structure of the wake is shown to depend primarily on the Strouhal number. At low St , a single-row wake occurs while at high St a double-row wake is observed at all simulated Re . Our results suggest that the St range within which the transition from the single- to the double-row wake structure occurs depends on the Reynolds number and the swimming mode.

In the comparisons of the anguilliform and carangiform virtual swimmers presented in this work, both the body morphology and

kinematics were different. Therefore, the present work cannot conclusively determine whether the differences we found in swimming performance are due to form or kinematics. It is reasonable to anticipate that both morphology and kinematics should play a role but to what extent each factor contributes is not known. In our future work, we will quantify the effects of each variable in the performance of these two modes of swimming by carrying out self-propelled simulations of a lamprey swimming like a mackerel and a mackerel swimming like a lamprey. These simulations are underway and will be reported in a future communication.

LIST OF SYMBOLS AND ABBREVIATIONS

a	amplitude envelope of lateral motion
A	width of the wake
a_{\max}	maximum amplitude
C_F	force coefficient
\bar{C}_F	mean axial force coefficient
CT	computed tomography
D	drag
EBT	Lighthill's elongated body theory
f	tail-beat frequency
F	force exerted on the fish body by the flow
F_D	drag force
F_L	lift force
h	lateral excursion of the body
\dot{h}	time derivative of the lateral displacement
HCIB	hybrid Cartesian/immersed-boundary
k	wave number of the body undulations
L	fish length
PIV	particle image velocimetry
\bar{P}_{side}	mean power loss
Re	Reynolds number
S	fish surface area
St	Strouhal number
St^*	critical Strouhal number
t	time
T	thrust
\bar{T}	mean thrust force
U	swimming speed
V	speed of the backward undulatory body wave
z	axial (flow) direction measured along the fish axis from the tip of the fish's snout
β	slip velocity
η	Froude propulsive efficiency
η_{EBT}	Froude efficiency based on the elongated body theory
λ	wavelength
ν	kinematic viscosity of the water
ρ	fluid density
τ	tail-beat period
τ_{ij}	viscous stress tensor
ω	angular frequency

This work was supported by NSF Grants 0625976 and EAR-0120914 (as part of the National Center for Earth Surface Dynamics) and the Minnesota Supercomputing Institute. We are grateful to Professor Smits at Princeton University for providing the lamprey morphology data from the CT data of Professor Fish. Thanks to Ehsan Borazjani for creating the lamprey geometry and the triangular mesh with Ansys.

REFERENCES

- Anderson, E., McGillis, W. and Grosenbaugh, M. (2001). The boundary layer of swimming fish. *J. Exp. Biol.* **201**, 81-102.
- Bainbridge, R. (1958). The speed of swimming of fish as related to size and to the frequency and amplitude of the tail beat. *J. Exp. Biol.* **35**, 109.
- Balay, S., Buscheiman, K., Eijkhout, V., Gropp, W. D., Kaushik, D., Knepley, M.G., Curfman McInnes, L., Smith, B. F. and Zhang, H. (2004). PETSc User Manual, Argonne National Laboratory Report No. ANL-95/11 – Revision 2.1.5.
- Barrett, D. S., Triantafyllou, M. S. and Yue, D. K. P. (1999). Drag reduction in fish-like locomotion. *J. Fluid Mech.* **392**, 183.
- Borazjani, I. (2008). Numerical simulations of fluid-structure interaction problems in biological flows. PhD Thesis, Mechanical Engineering Department, University of Minnesota, Minneapolis, MN, USA.

- Borazjani, I. and Sotiropoulos, F.** (2008). Numerical investigation of the hydrodynamics of carangiform swimming in the transitional and inertial flow regimes. *J. Exp. Biol.* **211**, 1541-1558.
- Borazjani, I., Ge, L. and Sotiropoulos, F.** (2008). Curvilinear immersed boundary method for simulating fluid structure interaction with complex 3D rigid bodies. *J. Comput. Phys.* **227**, 7587-7620.
- Buchholz, J. H. J. and Smits, A. J.** (2008). The wake structure and thrust performance of a rigid low-aspect-ratio pitching panel. *J. Fluid Mech.* **603**, 331-365.
- Carling, J. and Williams, T. L.** (1998). Self-propelled anguilliform swimming: simultaneous solution of the two-dimensional Navier–Stokes. *J. Exp. Biol.* **201**, 3143-3166.
- Cheng, J. Y. and Blickhan, R.** (1994). Note on the calculation of propeller efficiency using elongated body theory. *J. Exp. Biol.* **192**, 169-177.
- Dabiri, J. O.** (2005). On the estimation of swimming and flying forces from wake measurements. *J. Exp. Biol.* **208**, 3519-3532.
- Donley, J. M. and Dickson, K. A.** (2000). Swimming kinematics of juvenile kawakawa tuna (*Euthynnus affinis*) and chub mackerel (*Scomber japonicus*). *J. Exp. Biol.* **203**, 3103-3116.
- Fish, F. E.** (1993). Power output and propulsive efficiency of swimming bottlenose dolphins (*Tursiops truncatus*). *J. Exp. Biol.* **185**, 179-193.
- Fish, F. E. and Lauder, G. V.** (2006). Passive and active flow control by swimming fishes and mammals. *Annu. Rev. Fluid Mech.* **38**, 193.
- Fish, F. E., Innes, S. and Ronald, K.** (1988). Kinematics and estimated thrust production of swimming harp and ringed seals. *J. Exp. Biol.* **137**, 157-173.
- Ge, L. and Sotiropoulos, F.** (2007). A numerical method for solving the 3D unsteady incompressible Navier–Stokes equations in curvilinear domains with complex immersed boundaries. *J. Comput. Phys.* **225**, 1782-1809.
- Gilmanov, A. and Sotiropoulos, F.** (2005). A hybrid cartesian/immersed boundary method for simulating flows with 3D, geometrically complex, moving bodies. *J. Comput. Phys.* **207**, 457.
- Gray, J.** (1933a). Studies in animal locomotion II. The relationship between waves of muscular contraction and the propulsive mechanism of the eel. *J. Exp. Biol.* **10**, 386-390.
- Gray, J.** (1933b). Studies in animal locomotion. I. The movement of fish with special reference to the eel. *J. Exp. Biol.* **10**, 88-104.
- Hultmark, M., Leftwich, M. and Smits, A.** (2007). Flowfield measurements in the wake of a robotic lamprey. *Exp. Fluids* **43**, 683.
- Hunt, J. C. R., Wray, A. A. and Moin, P.** (1988). Eddies, streams, and convergence zones in turbulent flows. In *Studying Turbulence Using Numerical Simulation Databases, 2. Proceedings of the 1988 Summer Program, (SEE N89-24538 18-34)*, pp. 193-208. Stanford, CA: Summer Program, June-July 1988.
- Kern, S. and Koumoutsakos, P.** (2006). Simulations of optimized anguilliform swimming. *J. Exp. Biol.* **209**, 4841.
- Koochesfahani, M. M.** (1989). Vortical patterns in the wake of an oscillating airfoil. *AIAA Stud. J.* **27**, 1200.
- Lauder, G. V. and Tytell, E. D.** (2006). Hydrodynamics of undulatory propulsion. *Fish Physiol.* **23**, 425-468.
- Lighthill, M. J.** (1960). Note on swimming of slender fish. *J. Mech.* **9**, 305.
- Lighthill, M. J.** (1969). Hydromechanics of aquatic animal propulsion. *Annu. Rev. Fluid Mech.* **1**, 413-446.
- Lighthill, M. J.** (1970). Aquatic animal propulsion of high hydromechanical efficiency. *J. Fluid Mech.* **44**, 265.
- Lighthill, M. J.** (1971). Large-amplitude elongated-body theory of fish locomotion. *Proc. R. Soc. Lond. B, Biol. Sci.* **179**, 125.
- Lindsey, C. C.** (1978). Form, function, and locomotory habits in fish. In *Fish Physiology* (ed. W. S. Hoar and D. J. Randall), pp. 1-100. New York: Academic Press.
- Liu, H. and Kawachi, K.** (1999). A numerical study of undulatory swimming. *J. Comput. Phys.* **155**, 223.
- Muller, U. K., Van Den Heuvel, B. L. E., Stamhuis, E. J. and Videler, J. J.** (1997). Fish foot prints: morphology and energetics of the wake behind a continuously swimming mullet (*Chelon labrosus* Risso). *J. Exp. Biol.* **200**, 2893-2906.
- Muller, U. K., Smit, J., Stamhuis, E. J. and Videler, J. J.** (2001). How the body contributes to the wake in undulatory fish swimming: flow fields of a swimming eel (*Anguilla anguilla*). *J. Exp. Biol.* **204**, 2751-2762.
- Muller, U. K., van den Boogaart, J. G. M. and van Leeuwen, J. L.** (2008). Flow patterns of larval fish: undulatory swimming in the intermediate flow regime. *J. Exp. Biol.* **211**, 196.
- Nauen, J. C. and Lauder, G. V.** (2002). Hydrodynamics of caudal fin locomotion by chub mackerel, *Scomber japonicus* (Scombridae). *J. Exp. Biol.* **205**, 1709.
- Rosen, M. W.** (1959). Water flow about a swimming fish. PhD thesis, US Naval Ordnance Test Station, China Lake, CA, USA.
- Saad, Y.** (2003). *Iterative Methods for Sparse Linear Systems*. Philadelphia: SIAM.
- Schultz, W. W. and Webb, P. W.** (2002). Power requirements of swimming: do new methods resolve old questions? *Integr. Comp. Biol.* **42**, 1018-1025.
- Sfakiotakis, M., Lane, D. M. and Davies, J. B. C.** (1999). Review of fish swimming modes for aquatic locomotion. *IEEE J. Ocean. Eng.* **24**, 237.
- Shen, L., Zhang, X., Yue, D. K. P. and Triantafyllou, M. S.** (2003). Turbulent flow over a flexible wall undergoing a streamwise travelling wave motion. *J. Fluid Mech.* **484**, 197.
- Triantafyllou, M. S. and Triantafyllou, G. S.** (1995). An efficient swimming machine. *Sci. Am.* **272**, 64.
- Triantafyllou, M. S., Triantafyllou, G. S. and Yue, D. K. P.** (2000). Hydrodynamics of fishlike swimming. *Annu. Rev. Fluid Mech.* **32**, 33-53.
- Tytell, E. D.** (2004). Kinematics and hydrodynamics of linear acceleration in eels, *Anguilla rostrata*. *Proc. R. Soc. Lond. B, Biol. Sci.* **271**, 2535-2540.
- Tytell, E. D.** (2007). Do trout swim better than eels? Challenges for estimating performance based on the wake of self-propelled bodies. *Exp. Fluids* **43**, 701-712.
- Tytell, E. D. and Lauder, G. V.** (2004). The hydrodynamics of eel swimming I. Wake structure. *J. Exp. Biol.* **207**, 1825.
- Videler, J. J.** (1993). *Fish Swimming*. London: Chapman and Hall.
- Videler, J. J. and Wardle, C. S.** (1991). Fish swimming stride by stride: speed limits and endurance. *Rev. Fish Biol. Fish.* **1**, 23.
- Wolfgang, M. J., Anderson, J. M., Grosenbaugh, M. A., Yue, D. K. and Triantafyllou, M. S.** (1999). Near-body flow dynamics in swimming fish. *J. Exp. Biol.* **202**, 2303-2327.